DOI:10.14753/SE.2022.2605

MECHANICAL CHARACTERIZATION OF WEAK, ELECTROSPUN AND BIOLOGICAL FIBER TEXTURE

Ph.D. thesis

Evelin Forró

Doctoral School of Theoretical and Translational Medicine

Semmelweis University

Supervisor: Miklós Zrínyi, PhD, MTA member

Official reviewers: Rita Kiss, PhD, MTA member
Ákos Zsembery, MD, PhD

Head of the Complex Examination Committee:

György Losonczy, MD, DSc

Members of the Complex Examination Committee:

Janina Kulka, MD, DSc
Lajos Géczi, MD, PhD

Budapest
2021

DOI:10.14753/SE.2022.2605

TABLE OF CONTENTS

DOI:10.14753/SE.2022.2605

DOI:10.14753/SE.2022.2605

LIST OF ABBREVIATIONS

CDF	cumulative distribution function
ECM	extracellular matrix
FBM	fiber bundle model
FFT	fast fourier transform
HL	hidden length
PDF	probability density function
PSI	polysuccinimide
PVA	poly(vinyl-alcohol)
SB	sacrificial bond
SBHL	sacrificial bond and hidden length
SEM	scanning electron microscopy

DOI:10.14753/SE.2022.2605

1. INTRODUCTION

Many biological materials have complex fibrillary structure in nature, which plays a central role in their mechanical properties. Biopolymer fibers have a decisive role in many natural materials like in spider web [1-3], hairs [4-6], tendons and soft connective tissue, such as arterial walls and cellular cytoskeleton. The extracellular matrix (ECM) is also an important structural component of tissue, in which the fiber web is responsible for sustaining planar stresses in all direction [7,8].

Synthesis of protein-like nano- and microfibers, capable of mimicking biological functions is the ultimate challenge to modern science A growing need for the production of artificial biological tissues dictates the production of model fibrous matrix with adequate properties. The development of sub-micrometer-sized biocompatible fibrous scaffold with improved chemical and mechanical properties could be of great promise in several biomedical applications due to the tailor-made synthetic nature, extreme purity, and possibility of production on a large scale [9,10].

The medical-biotechnological field of tissue engineering encompasses the development, preparation, and modification of implants. The development of polymer systems that facilitate the mechanical and cellular regeneration of tissue is a crucial task. Current strategies include the application of materials that are highly hydrated and its nanofibrous structure provides an ideal scaffold for the cells to colonize [11]. The development of novel artificial tissues composed of poly(amino acid)-based fibers may result in new techniques with improved efficiency [12-14].

Electrospun nano- and micro-fiber networks as novel materials have attracted an intensive research area over the past decades. Fibrous materials are becoming important technological applications due to their high mechanical performance and low weight. However, the electrospinning technology is well developed [15-19] and few studies are available on the mechanical performance of fibrous structures [20-25], little is known on the deformation mechanism and rigidity of spun fabrics despite of the fact that strength and load bearing capacity of these materials are important factors for several technological and biomedical applications. There is little understanding on how spun fabrics deform and fail under mechanical load. The mechanical properties of the fiber assemblies depend on the physical properties of single fibers as well as the geometrical arrangement [21,26]. Ordered or random structures of nano- and microfibers are highly

valuable in several technological areas as thin nearly planar fibrous systems like webs, sheets, yarn tangles [27-30], papers [31], woven and knitted textiles [32,33].

The mechanical behavior of fibrous materials deviates significantly from traditional materials because of the discontinuous nature of randomly distributed fibers. It is therefore important to know how microscopic failure processes (for example rupture or slipping of overloaded fibers) gives rise to macroscopic deformation.

1.1. The manmade and biological fiber networks

Many manmade and biological materials gain their strengths and toughness through fibrous structure. Paper is one of the oldest manmade random fiber network, made of cellulose fibers. In paper the fibers are densely packed and bonded by hydrogen bridges [31].

In the living organism an intercellular substance has formed for cell proliferation, which provide flexible, but mechanically resistant scaffold for the cells, this is the ECM [34]. ECM is a non-cellular three-dimensional macromolecular network filled with large amounts of fluid, composed of collagens, proteoglycans/glycosaminoglycans, elastin, fibronectin, laminins, glycoproteins [35]. In addition to these macromolecules, it also contains other types of proteins, hormones, and growth factors that generally promote cell adhesion, differentiation, and proliferation [35-39]. Due to its structure, the ECM is permeable to small molecules, flexible and responsive to changes in the environment, thus not only supporting, but also providing information and material flow (nutrients, degradation products) between cells [40].

The ECM consists of a large variety of macromolecules, which are fibrous forming proteins such as collagens, elastin, fibronectin, laminins, glycoproteins, proteoglycans and glycosaminoglycans. These molecules are highly acidic and hydrated. The composition and specific structure of the ECM vary from tissue to tissue [41].

The collagen fiber architecture plays a critical role in the biomechanical behavior of an ECM scaffold. The mechanical properties of the ECM depend on the alignment and organization of collagen fibers, which are also dependent on the function of the source tissue [41]. For example, the collagen fibers are highly aligned along the long axis in tendon or ligament to provide the greatest resistance against strain [42,43]. In other tissues the ECM has a layered structure in which every layer has its own fiber alignment, but the

tissues layers can be separated to measure the collagen fiber system with different directions. Biaxial mechanical testing showed that the structural differences changed the mechanical behavior of the resulting ECM scaffolds. The longitudinally separated material showed highly anisotropic behavior and the circumferentially separated material showed more isotropic behavior. [41,44].

These results help us to understand the relationship between the collagen fiber alignment and the mechanical behavior, which is essential to create an artificial tissue scaffold which is significantly similar in structure and mechanical properties to the natural ECM.

1.2. Material selection of the scaffold

The selection of materials from which fibers can be prepared is rather wide, including both inorganic and organic materials, such as metals [45-47], oxides [48-50], glass [46,51,52] and any synthetic polymers [53-56]. The selection of material is predominantly based on the particular application.

1.2.1. Preparation of polysuccinimide (PSI)

For creation of an ECM like artificial tissue scaffold a biocompatible and biodegradable polymer is needed. The poly(amino acids) meet these requirements, in which the polymer chain is composed exclusively of amino acids found in living organisms, so that it can be broken down by cells, used as a nutrient, and does not elicit an immune response in the cells.

Interest in poly(amino acids) began in the second half of the 19th century, when the first successful attempts were made to produce aspartic acid-based polymers. Schaal was the first to thermally bond aspartic acid molecules in 1871 [57]. He was followed by Schiff in 1897, who was able to combine four and then eight monomer units initially. He already used the collective name poly(aspartic acid) for the resulting tetra and octaaspartic acid [58]. Later, Frankel and Berger synthesized α-poly(aspartic acid) using N-carboxyanhydride method [59]. In the 1950s, Harada developed several methods for synthesizing poly(aspartic acid). First, by copolymerizing maleic acid amine and maleic acid, and then from a mixture of monoammonium fumaric acid and malic acid, it was possible to produce poly(aspartic acid) with a low degree of polymerization [60]. József

Kovács, Imre Könyves and Árpád Pusztai were the first to produce poly(aspartic acid) via PSI by a thermal process in 1953 [61].

PSI is the anhydrous form of poly(aspartic acid), which transformation can take place in the body, so PSI is ideal for medical application [12,62].

1.3. Electrospinning

Several techniques are available to prepare porous and fibrous structure for biomedical applications, such as drawing and phase separation, but the most common method is electrospinning. In this technique several materials can be used, and it allows to create polymer fibers with diameters varying from nm to μm [63-65].

Electrospinning technique was invented by Formhals in 1934, who applied electrical field to impose a uniaxial stretching of a viscoelastic jet derived from the polymer solution. This continuously reduce the diameter and leads to form nanofibers [15].

The schematic image of an electrospinning instrument can be seen in Fig. 1, the main parts of which are a syringe filled with the polymer solution, a pump to ensure an even flow of the solution, and a collector where the polymer nanofibers can be collected. A high DC voltage is essential for this technique. The positive electrode is attached to the metal needle tip of the syringe, while the negative electrode (ground) is attached to the collector in front of the needle. When a DC voltage is applied, the fibers are leaving the syringe, the polymer solution flies towards the collector with a whipping motion, meanwhile the solvent evaporates, so on the collector a solvent-free polymer nanofiber network is formed [15-18].

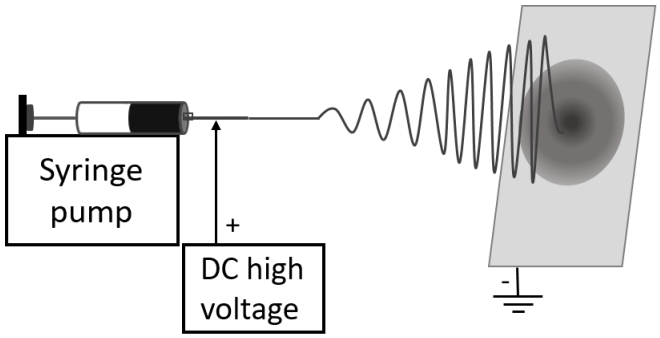

Figure 1: Schematic image of an electrospinning instrument.

1.4. Mechanical properties of fiber mats

Nowadays the technology to prepare fibers from several materials is developing rapidly. Despite the number of experimental studies on fundamental mechanical properties can be found in the literature rather rare [15,21,23,24,53,54,56,66].

The mechanical properties of planar fiber networks highly depend on the interactions between the fibers. With increasing number of contact points between electrospun fibers, the fiber-fiber adhesion force increases [67]. These interactions between the cross-lapping fibers include non-bonded van der Waals interactions that are responsible for the resistance against deformation. Whenever a contact point experiences a force equal to or greater than its strength threshold, it breaks. Similar effects can happen during debonding and slipping of stick fibers due to stretching [68].

Every breakage of contact point is detectable and countable in the loading curve, and two model can describe the mechanical properties of this fibrous structure, the Sacrificial bond and hidden length model, and the Fiber Bundle Model.

1.4.1. Sacrificial bond and hidden length (SBHL) model

Many biological and polymeric materials gain their strength and toughness from the combinations of organic and inorganic components [69-72], which provide a reversible, molecular-scale energy-dissipation mechanism [73]. In some natural materials, for example bone [74-79], abalone shells [80,81] and diatoms [82-84], the molecules possess a reversible toughening mechanism which greatly increase the fracture toughness of biomaterials [74,77,85]. This model is equivalent with the cooperation between weak bonds, which is widely used in the mechanical studies of fibrous materials [86,87].

The hierarchical structure of bone includes hydroxyapatite-impregnated twisted collagen fibrils, collagen fibers and a lamellar structure of collagen fibers. The mineralized collagen fibrils are interconnected by a special protein-based “glue” which is composed of polymer chains with SBHL systems [75,76,88]. In bone, and other biomaterials, this so-called glue molecule may include more than one polymer chain with SB-s which are forming within the chain itself, crosslinking the different chains and connecting the chains to the collagen fibrils (Fig. 2) [88]. Order of magnitude calculations

evidence that less than 1% by weight of this "glue" can have profound effects on the fracture resistance, because of SBHL [75,76].

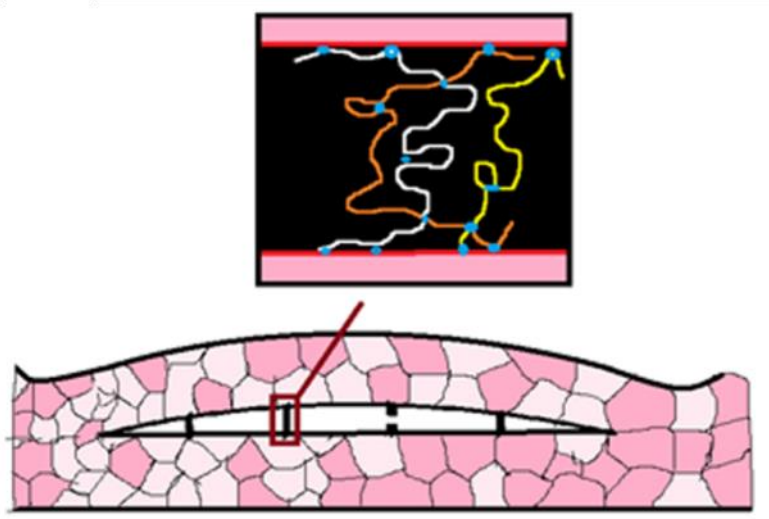

Figure 2: Hypothesized structures of assembled glue molecules, with SB-s (blue circles) along the backbone of the polymer molecules [88].

SB-s are defined as bonds that break before the molecular backbone is broken, because these bonds are frequently weaker than the covalent bonds of the main structure [74]. The hidden length is the part of the molecule that was covert from external forces by the SB [73]. In these networks of cross-linked molecules, large amounts of length can be hidden from an applied load by a variety of cross-links, including SB-s and entire cross-linking molecules as well [73].

The SBHL system provide a reversible, molecular-scale energy-dissipation mechanism which greatly increases the energy needed to break the material [74,77,85]. This system dissipates large amounts of energy with entropic and enthalpic forces while stretching out the hidden length of the “glue” molecules which is exposed when SB-s break [74]. The energy-dissipation during stretching allows to protect strong molecular bonds from irreversibly breaking, as the SB-s are much weaker than the bonds holding the structure together, so this will break first [76]. Another interesting property of the SB-s that they can form and open reversibly, because they based on multivalent cations cross-linking negatively charged molecules [74,76,89,90]. Recent atomic force microscopy experiments evidence that the behavior of soft matrix is governed by electrostatic interactions between negatively charged proteins and divalent Ca^{2+} ions

[76,91], so the effectiveness of the energy-dissipation mechanism increases with the presence of Ca^{2+} ions [76].

1.4.1.1. The breakage of a network with SB-s

First let's see what happens when there is only one SB. During the stretching the weakest SB breaks first (Fig. 3 (a)), which unravels the corresponding hidden length, and causing a force drop as an immediate result of the spike in entropy (Fig. 3 (b)) [73,88,92].

Initially, when the SB (star) is intact, only the entropy of the polymer (black part) contributes to the entropic spring (Fig. 3 (a)). As the force on the polymer increases and the breakage force of the SB is reached, it breaks which results in a drop in the force (Fig. 3 (b)). This force is typically around 300 nN [73]. After the breakage, the HL (red part) is released and from now the change of entropy of this part also contributes to the entropic spring of the polymer, so more work is needed against the change of entropy to stretching the polymer further (Fig. 3 (c)) [88,92].

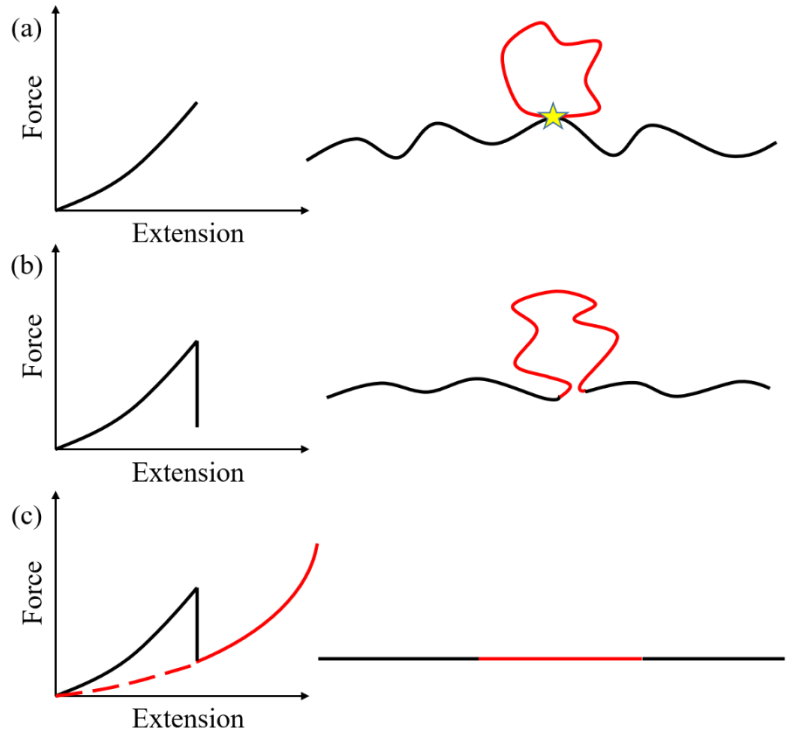

Figure 3: Schematic drawing of the basic principles of the SBHL mechanism. The star indicates the SB, and the red part represents the HL [92].

This is a self-healing mechanism, that means it could be reversible. When the force is relaxed, entropy collapses the polymer, and SB-s could reform [73].

When multiple SB-s with hidden length are present in a molecule, obviously multiple peaks appear in the force-extension curve, as it can be seen in Fig. 4, and the amount of dissipated energy is increased by the existence of several SBHL domains [73,88].

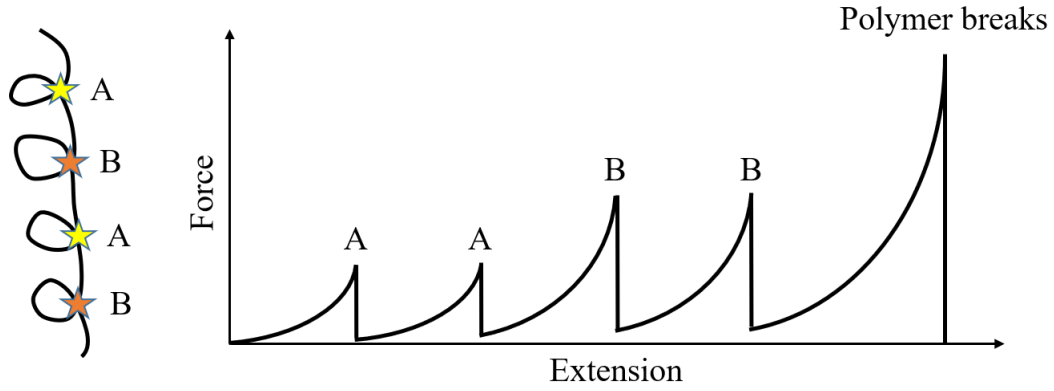

Figure 4: The schematic mechanical curve of a polymer with multiple SB-s with different strength, which is indicated by A and B letters [73].

If there are multiple polymer chains in a network with multiple SBHL system, the collective behavior of a group of polymer chains can be investigated, in which the force-extension curve looks smoother and maximum force increases as the number of chains (N_p) increases (Fig. 5) [88]. It is similar to the cohesive laws routinely used in fracture mechanics [93,94].

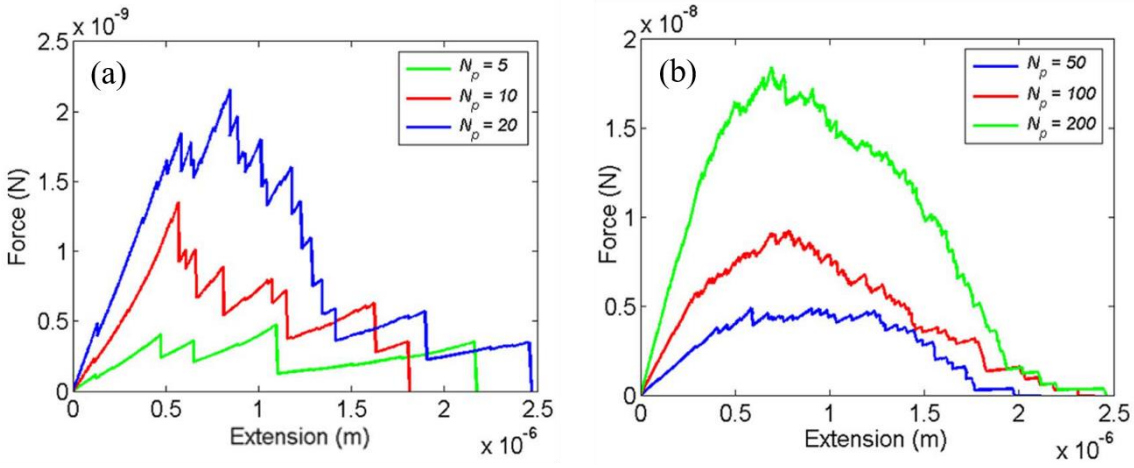

Figure 5: Representative curves illustrating force-extension response for: 5, 10, 20 (a) and 50, 100, 200 polymers (b) [88].

A saw-tooth like behavior can be seen in the force-extension curves (Fig. 5) as deforming a material with SB-s in molecules, which corresponds to unfolding and detachment events of the SBHL systems mechanism [95]. A similar behavior has been found for parallel polyprotein dimers [84] and spider capture silk [96].

1.4.1.2. Effects of SBHL on mechanical properties

SB-s and HL improve the fracture-resisting properties, as an increase of the initial stiffness of the material, and increase fracture toughness of several composite materials [85,96]. The strength is given from the initial slope of the force-extension curve, which is significantly changes as the material contains SBHL system. A high strength means that the material deforms only a little under the applied load [97].

In Fig. 6 two force-extension curves can be seen, the gray one shows a material with SB-s where the initial slope of the curve is significantly steeper (dash-dotted line), than the slope (dotted line) of a material without sacrificial molecules (black curve) [73].

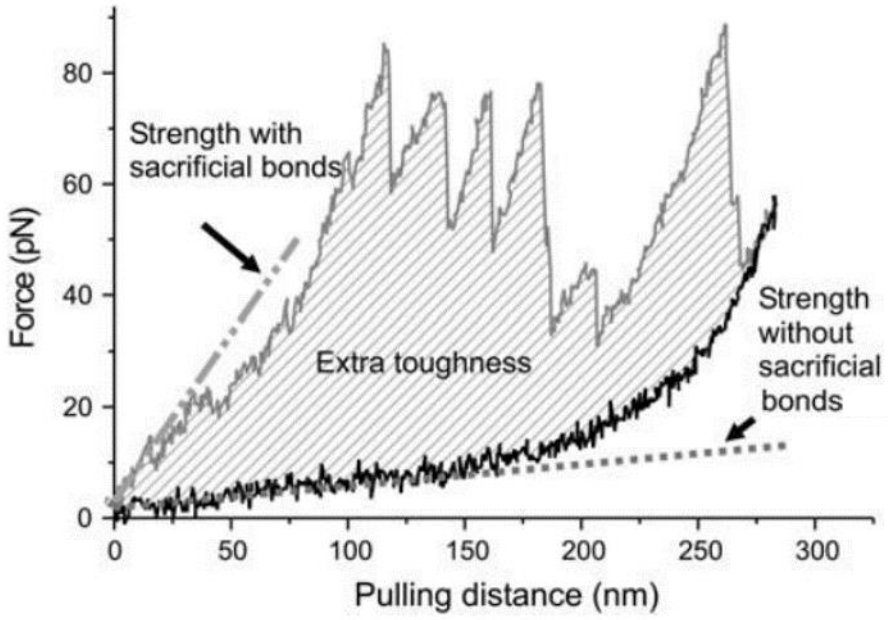

Figure 6: Loading curve of a material with SB-s (gray curve), and without SB-s (black curve) [73].

The shaded area in Fig. 6 shows the dissipated energy, which is significantly increase when deforming the material with SB-s, this is the extra toughness gained by the SBHL system [73].

The increased stiffness and toughness of materials resulting from the SBHL system mechanism is not only dependent on molecules with condensed domains within the molecule but rather on the presence of the shielded loops that are hidden from the applied force by SB-s [73].

A more complete understanding of this SBHL system mechanism can be useful in developing innovative therapeutic procedures. For example, this can help us to understand the changes in the bone mechanical response with aging, when the number of polymers produced by the osteocytes decreases, and therapeutic interventions can be suggested, which can help enhance bone mechanical behavior in the elderly [98,99]. The SBHL mechanism also must be considered in designing bio-inspired composite materials with improved fracture resistance properties, higher strength and toughness [88].

1.4.2. Fiber Bundle Model

The most accepted model of microscopic fracture mechanism is based on the Fiber Bundle Model (FBM) introduced by Peirce in 1926 to understand the strength of cotton yarns [100]. It considers how microscopic failure processes give rise to macroscopic deformation. This model was later modified and generalized in order to explain a variety of phenomena, including the damage and fracture caused by the breaking of fibers in mingled mats [101-104].

The Fiber Bundle Model envisages the material as a set of N_0 parallel, non-interacting fibers clamped at one end with an external load applied at the other end. The applied load is shared equally among the fibers. Each fiber is assumed to have identical spring constants κ but their breaking strengths are different. If the extension ε exceeds the rupture threshold, the fibers fail the weaker before the stronger. When the fiber bundle is loaded, certain overloaded fibers break according to their thresholds. If N_f fiber has failed at a certain extension , then the bundle experiences a force:

$$f = \kappa\,(N_0 - N_\mathrm{f})\,\varepsilon = N_0\kappa\left(1 - \frac{N_\mathrm{f}}{N_0}\right)\varepsilon \qquad (1)$$

The term $(1 - N_\mathrm{f}/N_0)$ denotes the fraction of fibers that are intact at extension ε. The quantity N_f/N_0 can be replaced by $F\,(\varepsilon)$, which means the cumulative distribution function (CDF) of breaking extensions. Thus, the loading force can be written as:

$$f = K_0\,[1 - F\,(\varepsilon)]\,\varepsilon \qquad (2)$$

The above expression says that shape of loading curve is directly related to the CDF of failures. The proportionality constant $K_0 = N_0\kappa$ is called initial stiffness, which characterizes the resistance against deformation in lack of any material failure. The $F\ (\varepsilon)$ cumulative distribution function is also defined by the probability density function (PDF) $f\ (\varepsilon)$ as:

$$F\ (\varepsilon_2) - F\ (\varepsilon_1) = \int_{\varepsilon_1}^{\varepsilon_2} f\ (\varepsilon)\ \mathrm{d}\varepsilon \tag{3}$$

Here ε can be considered as a random variable called load threshold of fibers. The $F\ (\varepsilon)$ CDF tells us the probability that random variable ε assumes a value less than or equal to a given ε^*.

There are several probability distribution functions, describing random experiments, whose outcome cannot be predicted with certainty (uniform, normal, exponential, Poisson, Student's, Gamma, and so on) [105].

DOI:10.14753/SE.2022.2605

2. OBJECTIVES

To understand and model the mechanical behavior of fibrous biological tissues I have prepared weak electrospun fiber systems in order to study the loading behavior of fibrous texture.

The main purpose of the thesis was to establish the characteristic load-displacement behavior of brittle fibrous scaffold prepared by electrospinning from PSI, as well as to study how the microscopic failure process gives rise to a macroscopic plastic deformation.

The objectives of the thesis were the followings:

1. to prepare planar, randomly oriented fibrous network from PSI by electrospinning technique and study the fiber mats morphology, which include the determination of the fiber's diameter, the examination of the surface and the orientation of the fibers
2. to measure the fundamental mechanical properties of the fiber networks and quantify the damage formation by determining the number and the magnitude of abrupt force drops
3. to analyze and understand the force-extension behavior of these fibrous structures by the Sacrificial Bond and Hidden Length model, and the Fiber Bundle Model
4. to determine the cumulative distribution function of failures, appearing on the loading curve as abrupt force drops during extension, and analyze them on the basis of Weibull distribution
5. to compare the mechanical behavior of these artificial fibrous mats with human tissue to justify the relevance of this study in the design of medical implants

DOI:10.14753/SE.2022.2605

3. RESULTS

3.1. Preparation of the samples

The investigated samples were made from PSI, which was synthesized from L-aspartic acid by thermal polycondensation, the exact method can be found in previous publications of the research group [10,12]. PSI was dissolved is DMF in a concentration 25 m/m% for electrospinning. 9 kV DC voltage was applied, the needle-collector distance was 15 cm and the flow rate was 1 ml/h. All figures and evaluations presented in this work belong to the randomly oriented samples.

3.2. Characterization of PSI electrospun fibers

3.2.1. Morphological analysis

Morphological analysis was performed in order to observ the fibrous structure of the prepared samples. A Jeol JSM 6380LA scanning electron microscope with an accelerating voltage of 10 kV was used to visualize the fibers. For the investigation, the samples were sputtered with gold for 1 min. The SEM images in Fig. 7 show three different PSI electrospun fibers and a magnified one used in characterization. The fibers have smooth surface, individual fibers build up the mats, no fusion can be seen.

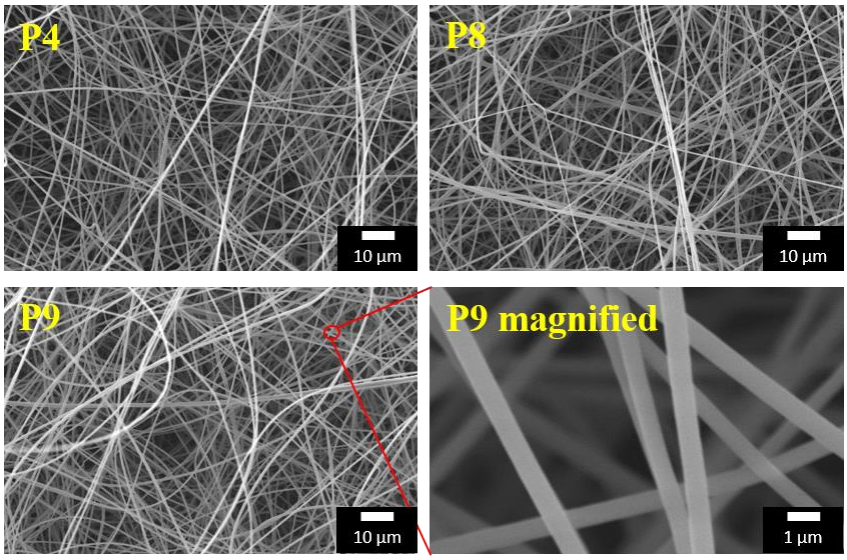

Figure 7: SEM images of three different PSI electrospun fibers and a magnified one used in characterization.

3.2.2. Determination of fiber diameter

The SEM images, shown in Fig. 7, were used to determine the diameter of the fibers. The average fiber diameter was calculated over 100 fibers taken from five different samples of the same condition by measuring the diameter of each fiber perpendicularly to its long axis. ImageJ analysis software was used for this purpose. I have found that a wide variety of fiber diameters occur within a sample, but the data of the different samples were similar. The average fiber diameter, which is representative for all sample, was found to be: 720±210 nm standard deviation.

3.2.3. Determination of fiber orientation

Quantification of the fiber alignment was determined from three images per each sample by applying the Fast Fourier Transform (FFT) of SEM images in ImageJ analysis software [26]. The FFT command computes the Fourier transform and displays the power spectrum from which the angle is expressed in degrees. The exact code can be found in the site of ImageJ [106,107].

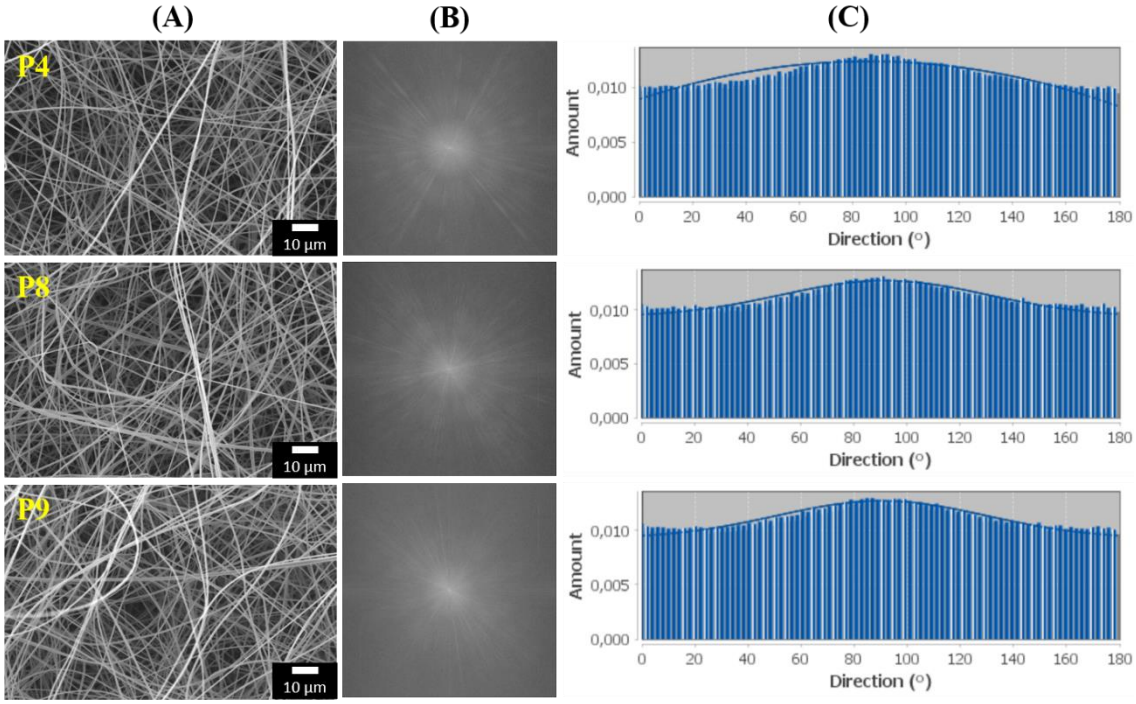

Figure 8: SEM images of the fibers (A), FFT output image (B), Directionality histograms (C): Amount of pixel intensity plot in function of the direction.

Based on the SEM images shown in Fig. 8 (A) FFT has been performed and shown in Fig. 8 (B). From these images, the software determines the orientation of the fibers by analyzing the intensity across the FFT image and create a histogram shown in Fig. 8 (C). These figures do not indicate definite alignment in the fiber mats, however a slight orientation against the director, between 80° and 100°, occurs.

3.3. Unidirectional stress-strain measurements

Strain-controlled unidirectional extension experiments were performed on several layers of the sheets. The samples were cut into rectangular specimens in different width and length with a razor. The sample considered to be a 2D network, as the thickness is negligible compared to the width and length. The distance between the two grips was 30 mm, which was considered to be the real length (h_0) for the calculation of strain. The tensile tests were performed by an Instron 5942 testing machine with a 50 N load cell. The load cell accuracy was found to be equal to or better than 0.25% of the indicated force. Fig. 9 shows the experimental set-up. All extension measurements were performed at room temperature. The measured data were analyzed with a MATLAB code.

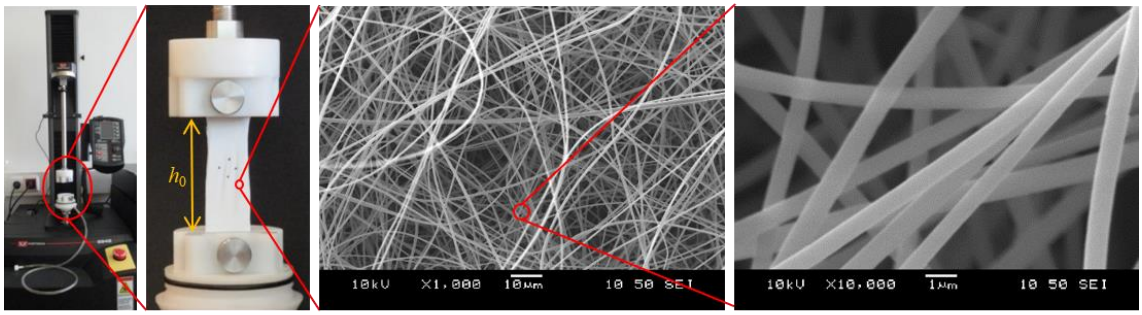

Figure 9: Strain controlled force measurements conducted by Instron 5942 equipment (a), the electrospun fiber mat under stretching (b), SEM picture showing the fibers (c) and (d).

A typical load–displacement curve of a sample is shown in Fig. 10. The experimental loading curve shows a symmetrical parabolic type dependence at large scales and saw tooth-like force–extension behavior at small scales.

The individual fibers are highly entangled and the layer is isotropic, therefor different level of interactions can occur in the texture. Geometrical limitations as well as

non-bonded interactions, such as van der Waals and electrostatic interactions, or entanglements, between the contact points of adjacent fibers restrict the movement of the fibers in the texture [67].

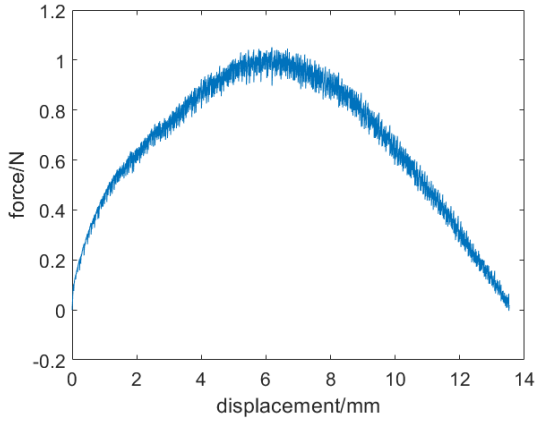

Figure 10: A typical load–displacement curve of a fiber mat.

The dependence of uniaxial deformation on the load is not linear; it goes through a maximum point. This symmetrical parabolic type dependence is expected on the basis of FBM under a uniform distribution of fiber strength [105]. On the other hand, the load–displacement curve shows quite high fluctuations in the direction of force. The amplitudes of the force fluctuations were found to be much larger than the experimental accuracy of the measurement.

Detailed analysis of the shape of the loading curves was carried out by enlarging the curves. Figure 11 shows magnified plots of the load–displacement curve of the sample shown in Fig. 10 in the displacement ranges of 0–2.5 mm (Fig. 11 (a)), 0–0.5 mm (Fig. 11 (b)), and 0–0.25 mm (Fig. 11 (c)). All magnified curves exhibit saw tooth-like force–extension behavior, which indicates damage; there are abrupt drops in force in the load–displacement curve, which are similar to the force drops of SBHL system mentioned in Chapter 1.4.1. The similarity to the SBHL model is not complete because here the FBM and the SBHL model prevail together. Figures 15 (c) and (d) are more similar to those described for the SBHL model. Thus, the material of the network and the adhesion forces between the fibers can also significantly contribute to the curve.

DOI:10.14753/SE.2022.2605

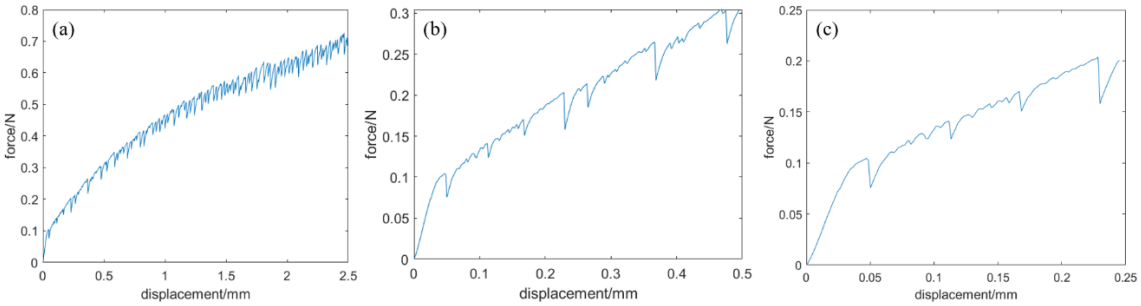

Figure 11: Enlarged view of the load–displacement curve of the sample shown in Fig. 10 in the displacement range of 0–2.5 mm (a), 0–0.5 mm (b), and 0–0.25 mm (c).

The force drop may be the consequence either of fiber rupture or of fiber slip, but at this point, it is difficult to differentiate the two cases, and both of them are considered as material damage. I can conclude that, these damages become "observable" and measurable by means of this experimental technique. Thus, it is possible to quantify damage formation by analyzing the measured load–displacement curves.

3.4. Determination of the rupture force

The statistical properties of rupture sequences during extension were also investigated by studying both the position and the strength distribution of rupture force. Numerical differentiation of the loading force as a function of displacement provides a better visualization of force drops (Δf), as shown in Fig. 12. The load–displacement curve shown in Fig. 11 (b) was used to create Fig. 12 with the equation below:

$$\Delta f = \frac{f(x_{i+1}) - f(x_i)}{x_{i+1} - x_i} \tag{4}$$

where x_i and x_{i+1} are the i-th and the (i+1)-th points of the displacement, $f(x_i)$ and $f(x_{i+1})$ are the detected forces at the i-th and the (i+1)-th displacement.

To establish the experimental error, first the $\Delta f \geq 0$ region was analyzed, where there are no force drops, just the fluctuation of the instrument occurs. This range was determined for each measured curve by analyzing the magnitude of the force changes in the positive direction. These values were slightly overestimated, and then averaged to ignore the very small fluctuations, that could be considered as errors, during the calculation of the ruptures. This mean was 7.1 mN/mm for this sample. Considering that,

the fluctuation on both sides of the force is governed by the same law, I found that the force randomly fluctuates in the range of $-7.1 \leq \Delta f_{\text{error}} \leq 7.1$ mN/mm (Fig. 12).

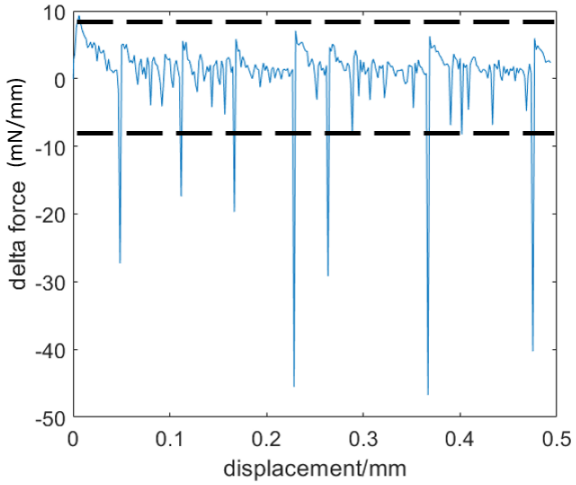

Figure 12: Force drop sequences calculated from Fig. 11 (b). The dashed line indicates the range of experimental error. Within this range, no force drops were considered.

This interval is considered to be the experimental error due to fluctuations. The negative force drops which exceed -7.1 mN/mm are accounted as damages in the sample. The magnitude of Δf was also determined by considering $\Delta f < \Delta f_{\text{error}}$. As evident from Fig. 12, the force drops caused by ruptures ($f_{\text{r}} = \Delta f - \Delta f_{\text{error}}$) varies from -10 to -50 mN/mm, and if *s* denotes the number of damages for a given elongation (0–0.5 mm), then *s* = 7 for the enlarged case shown in Figs. 11 (b) and 12.

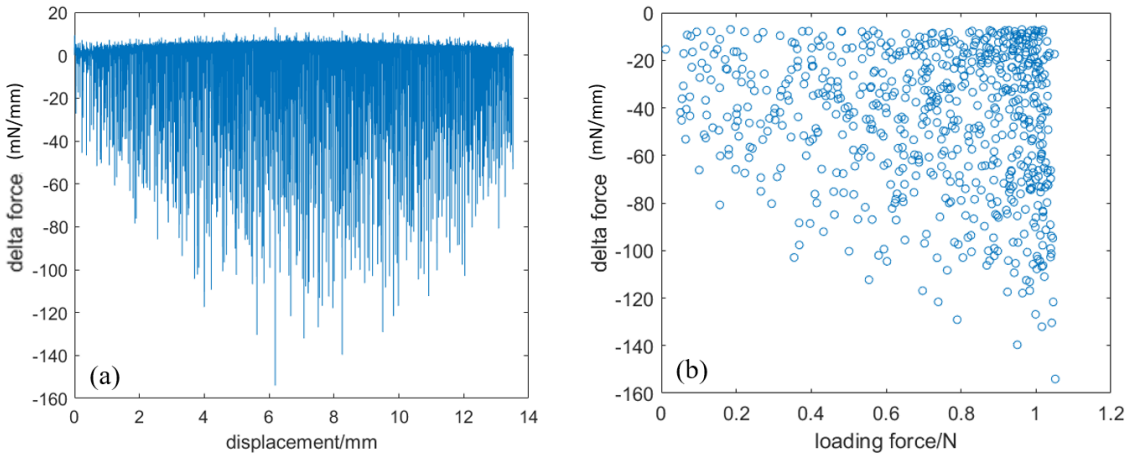

Figure 13: Delta force as a function of displacement (a) and of loading force (b) from the loading curve shown in Fig. 10.

The rupture force sequences for the entire loading curve, shown in Fig. 10, was determined, and the results are shown in Fig. 13 (a). The $(f, \Delta f)$ coordinates of the loading curve after subsequent ruptures can be seen in Fig. 13 (b). The figures indicate that both the appearance and the magnitude of the force drops seem to be random. The value of the correlation test was -0.163, which confirms that there is no correlation between the force drops and the loading force. Damages occur in the fiber bundle at the very beginning of the deformation and continue until all the fibers fail. I have found that the damage evolution increases as the elongation increases, and the range of force fluctuation increases with increase in the load. The force drops fluctuate between 0 and -160 mN/mm. These values suggest that the strength of individual fibers is different; each fiber has a different brittle response until it breaks. When the bundle is strained, the weakest fiber begins to rupture, followed by other fibers in the order of increasing strength. According to these results, a wide range of the spring constant has to be considered. According to recent theoretical approach nonlinear spring constant was defined. This allows to determine the number of ruptures as a function of stretching, as well as the magnitude of rupture force as a function of the applied loading force. In this sample, the force drops exceeding -7.1 mN was found to be s = 683.

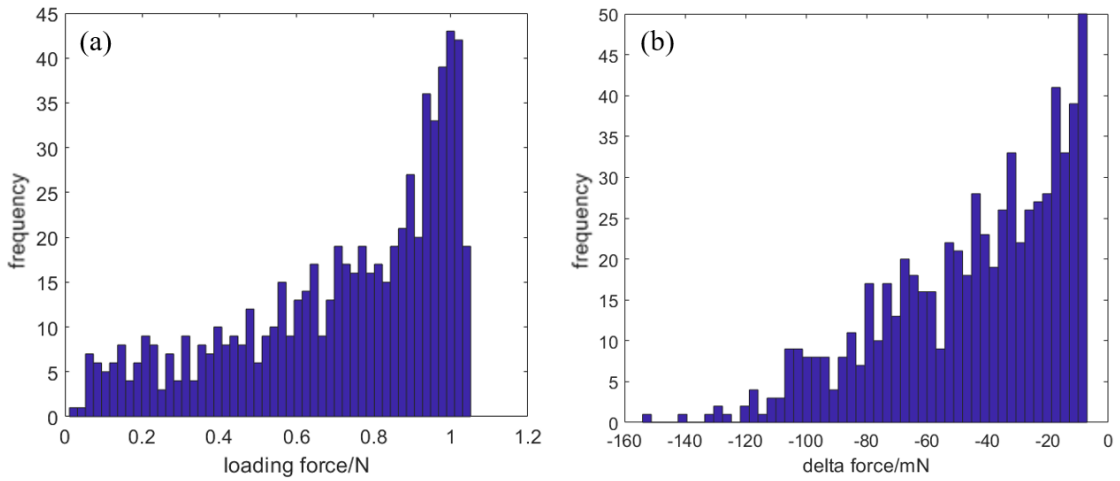

Figure 14: Frequency distribution of the number of ruptures at a certain loading force (a) and at a certain force drop (b) for rupture events.

To visualize the general characteristics of experimental data and to identify the different mechanical behavior, I summarized the experimental results by frequency distributions. Figure 14 (a) shows the number of ruptures at a certain loading force (f),

DOI:10.14753/SE.2022.2605

which indicates that as the loading force increases, the number of ruptures increases. Figure 14 (b) shows the number of ruptures at a certain delta force (Δf). According to this histogram, the smaller the delta force, the more ruptures occur, which indicates that, first, the available weaker bonds break.

DOI:10.14753/SE.2022.2605

4. DISCUSSION

4.1. Interpretation of the loading curve

In Fig. 15, several load-extension curves for weak fiber nets are shown. The material selection is rather diverse, a cospinning material includes hydrophilic: PVA and hydrophobic PSI weak fiber bundle. In addition to these loading curves an inorganic planar fiber network (aluminium-oxide: Al_2O_3) as well as a planar cotton fiber net are also shown. These figures inevitably illustrate that typical load curves for fiber mats are nonlinear; they all show maximum type dependence. Similar, maximum type load-displacement curves have been found for human tendon and other polymer fiber nets [108-110].

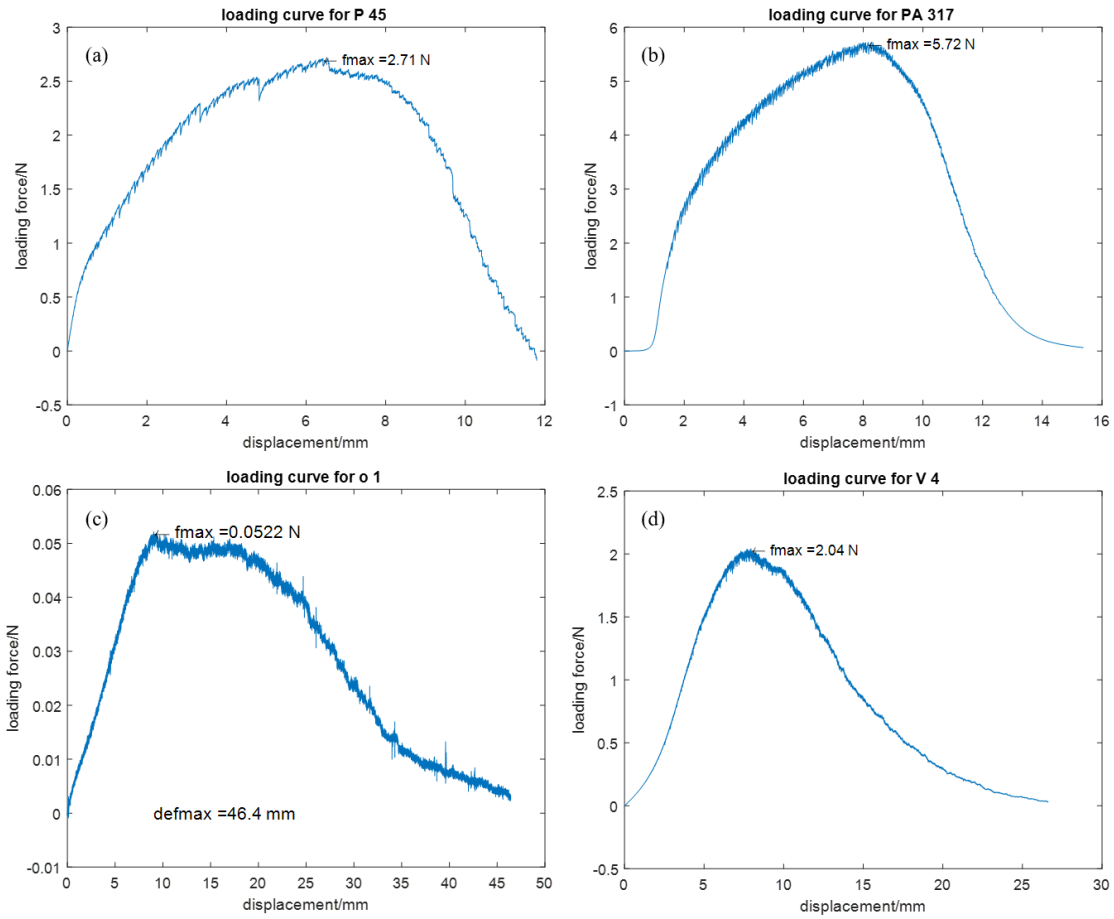

Figure 15: Typical load-displacement curves of dry fiber mats. Sample identification: P45: PSI (a), PA317: PSI-PVA (b), O1: aluminium-oxide (c), V4: cotton wool (d).

The typical character of all loading curves can be summarized as follows. At the very beginning of the applied load, the force has an approximate linear relationship in the low strain regime. The force has a maximum at a particular elongation, which characterizes the maximum strength of the whole fiber network. This point is often called as maximum loading capacity, the maximum force that the fiber net can stand. The knowledge of this point is important for any biomedical and technical application as well. When the elongation exceeds the deformation at maximum point, the force gradually decreases and finally goes to zero. It is generally accepted that this type of dependence is due to damage formation during deformation [101]. The other important remark is that the loading curves show quite high fluctuations in the direction of force [111].

I have found that the unusual loading curves shown in Figs. 10 and 15 are due to stiffness reduction, which is the consequence of failures, occurring during elongation. Since the individual fibers that build up the texture, have different breaking threshold, the force of overloaded fiber drops down to zero, and the remaining load has to be shared by the other intact fibers. As a result, the rest of the surviving fibers has to carry more load. The failures may be due to either breaking of fibers, or slipping from certain point of the fiber into another contact point. The observed force drops shown in Figs. 11 are the consequence of failures occurring during elongation. At the same time, they visualize the occurrence of material damage. At this point, we are not in the position to distinguish these basically different phenomena from each other. For the sake of simplicity, I use the general term for all: rupture for fiber-contact point debonding, fiber slips as well as real breaking. The experiments have evidenced that damage evolution is a consequence of strain induced force drops. It is possible to quantify the damage formation: determine the number, as well as the magnitude of force drops. I have made many mechanical measurements (see in Table I) in order to study the sawtooth-like force-extension behavior at short scale and maximum type loading curve dependence at large scale.

Several planar PSI textures were prepared for mechanical measurements collected in Table I. As the thickness of the samples is negligible compared to the width and length, the surface density was used for characterization of the samples. The loading curve was analyzed for each of the samples listed in Table I., as it is mentioned in Chapter 3.4. The rupture force sequences as well as the magnitude of the force drops were determined in the entire deformation range [112].

DOI:10.14753/SE.2022.2605

Table I: Characterization of PSI samples used for the measurements. Codes were used to identify de sample: P stands for PSI, and the number indicates the electrospun product.

Sample code	Elongation rate	Width	Initial length	Surface density
	mm/min	mm	Mm	g/m^2
P11	1	22.32	50.84	15.9
P12	1	18.9	67.28	21.6
P13	10	21.38	47.08	17.2
P22	0.5	24.92	54.82	36.6
P41	1	21.4	79.44	8.9
P42	1	25.8	64	10.2
P43	1	22.34	60.16	18.3
P45	0.5	22.36	59	16.8
P46	2	23	46.74	12.9
P63	1	13.54	51	11.4
P71	0.5	22.66	50.18	10.1
P72	1	21.88	51.48	23.8
P81	1	22.36	50.22	17.2
P83	1	14.94	49.56	22.3
P84	1	15	49.94	28.7
P85	1	28.74	51.46	19.4
P86	1	28.6	51.46	13.6
P87	1	22.78	15.86	25.9
P91	1	22.42	50.16	20.7
P701	1	21.68	50.96	19.6

These 20 samples are prepared with the same method, mentioned in Chapter 3.1., and measured as it is described in Chapter 3.3. The differences between the samples are summarized in Table I. I found that neither the elongation rate nor the size of the samples caused significant differences in the loading curves.

DOI:10.14753/SE.2022.2605

4.2. Determination of rupture sequences

From the numerous mechanical experiments listed in Table I., two samples were selected randomly to illustrate the whole evaluation method. These two samples are P83 and P701.

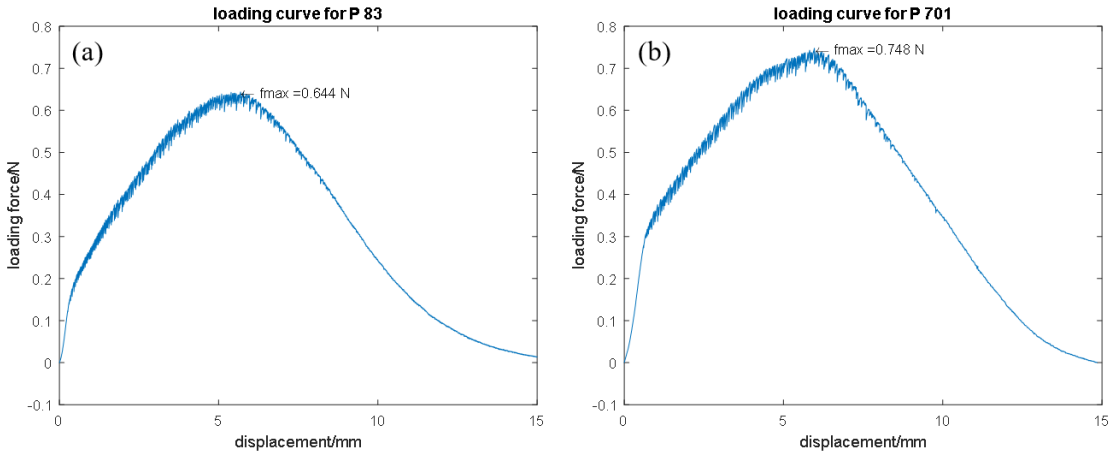

Figure 16: The loading curves of P83 (a) and P701 (b) samples.

Numerical differentiation of loading curves, shown in Fig. 16, with respect of extension provides the rupture sequences of each samples, can be seen in Fig. 17.

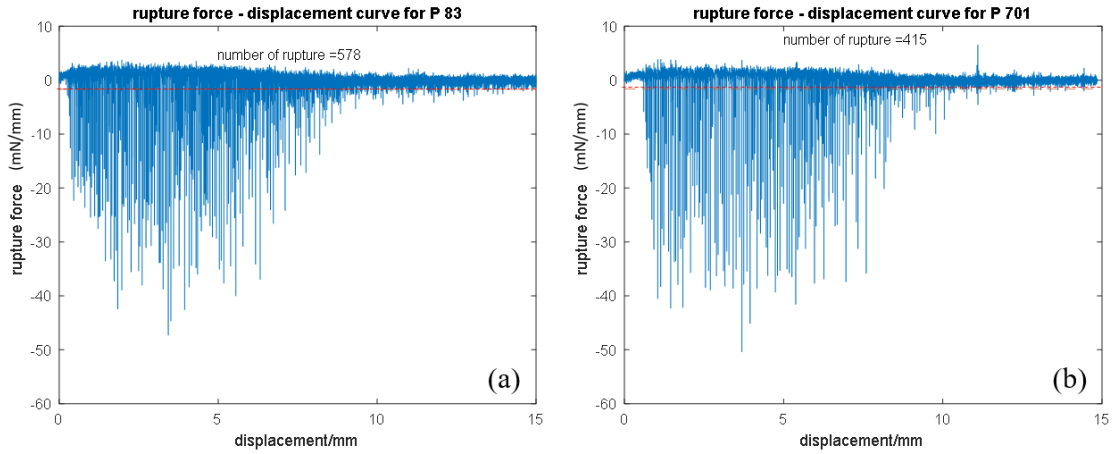

Figure 17: The rupture sequences of P83 (a) and P701 (b) samples. The red dashed line indicates the $\Delta f_{\mathrm{error}}$.

In order to separate the experimental error from the real force drops, the $\Delta f \geq 0$ region was determined on the derivative curve. Considering that in this range no force drops occur, the root of fluctuation is merely due to experimental uncertainty of the mechanical measurement. I have found that the force randomly fluctuates in the range of

$0 \leq \Delta f \leq 1.7$ mN/mm for the P83, and $0 \leq \Delta f \leq 1.6$ mN/mm for the P701 samples. Supposing that the fluctuations on both side of force governed by the same law, therefore $-1.7 \leq \Delta f_{\text{error}} \leq 1.7$ mN/mm and $-1.6 \leq \Delta f_{\text{error}} \leq 1.6$ mN/mm were considered to be the experimental error of the samples. Every negative force drop exceeds Δf_{error} was counted as rupture, so the number of ruptures was determined for each sample, and these values are shown in Table II. The magnitude of the rupture force was calculated by $f_{\text{r}} = \Delta f - \Delta f_{\text{error}}$, thus $f_{\text{r}} \geq 0$.

Based on Fig. 17, it is not possible to distinguish between the number of ruptures and magnitude of rupture force. To obtain these data the whole deformation regions were divided into equally distributed small bins. In this case, the bin size was 500, corresponding to 0.5 mm displacement (Figs. 18 and 19). Figures 18 and 19 show that neither the number of rupture nor the magnitude of their force follows uniform distribution., so our first task was to find the appropriate distribution for data evaluation.

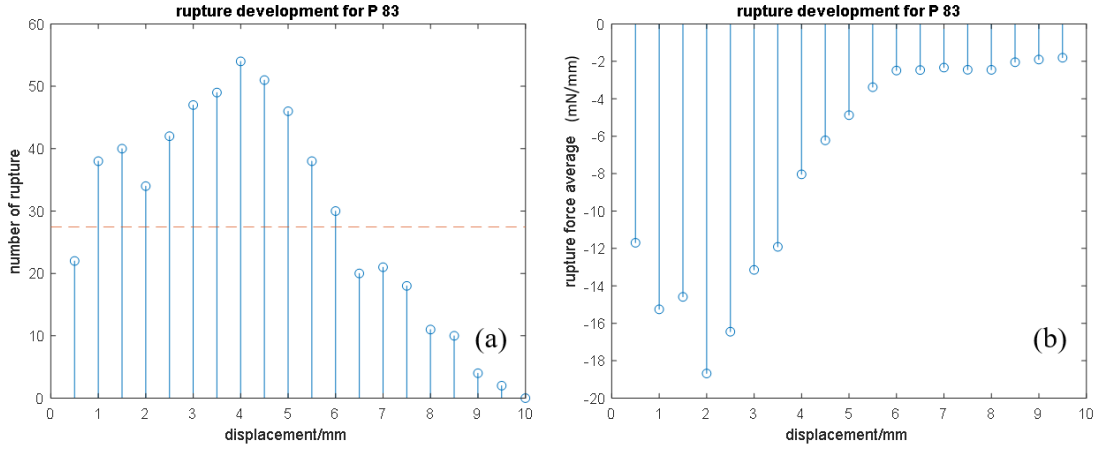

Figure 18: The number of ruptures (a) and magnitude of rupture force (b) as a function of displacement for P83 sample. Dashed line shows the average value.

DOI:10.14753/SE.2022.2605

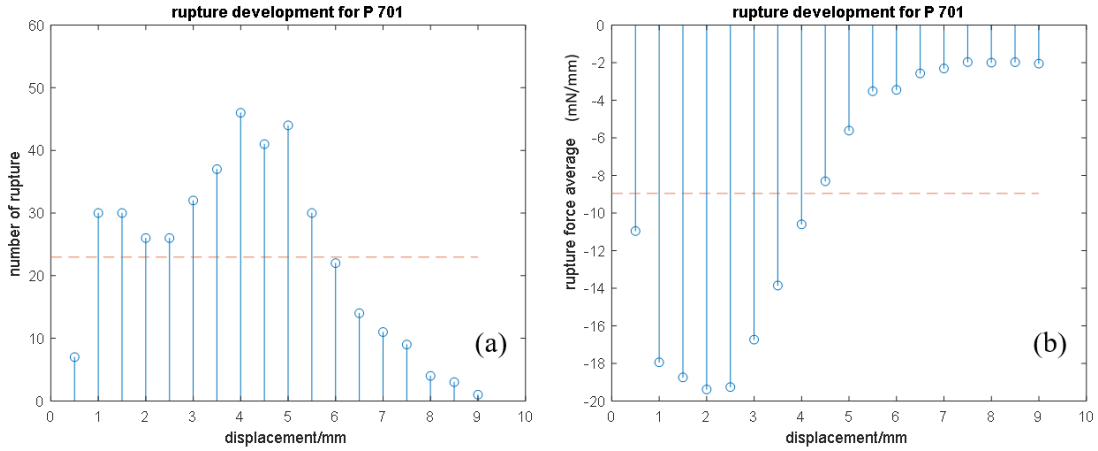

Figure 19: The number of ruptures (a) and magnitude of rupture force (b) as a function of displacement for P701 sample. Dashed line shows the average value.

Another interesting aspect of the mechanical failure of the studied fiber bundle: Are the subsequent rupture forces correlated? To answer this question, the rupture force against loading force was plotted in Figure 20.

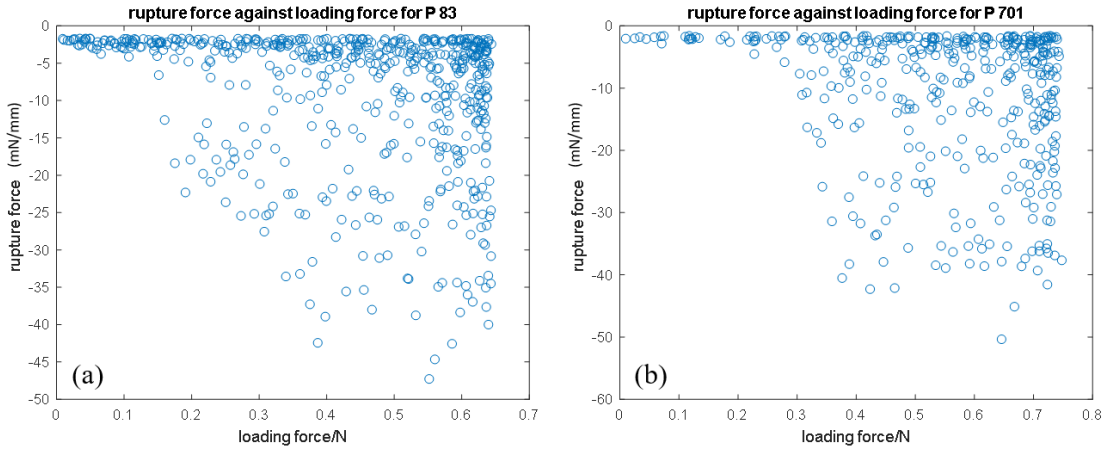

Figure 20: The rupture force against the loading force for P83 (a) and P701 (b) samples.

According to Fig. 20 and the value of the correlation test, which were 0.0132 for the P83 and 0.086 for the P701, no correlation between the force drops and the loading force can be found. This finding supports the random nature of force drops. I want to quantify with probability distribution the likelihood of the rupture force as a random variable. Recall from Chapter 1.4.2. the shape of loading curve (Eq. 2) is determined by the cumulative distribution function of failures.

4.3. Determination of the empirical cumulative distribution function of rupture force

I adopted the data from the rupture force sequences (Fig. 17) and determined the empirical cumulative distribution function according to the method described in ref [105].

This empirical distribution function is based on the order statistics. I ordered the individual rupture force data in ascending order. If the total number of ruptures is *n*, the order statistics is defined as:

$$f_{r,1} \leq f_{r,2} \leq f_{r,3} \leq \ldots . f_{r,i} \ldots . \leq f_{r,n} \quad (5)$$

where $f_{r,i}$ denotes the *i*-th rupture force in the order. For a discrete random variable, the empirical distribution function $F_e\ (f_r)$ is defined as [105]:

$$F_e\ (f_r) = {}^{i}/_{n};\ \text{if}\ f_{r,i} \leq f_r \leq f_{r,i+1} \quad (6)$$

In other cases, $F_e\ (f_r) = 0$; if $f_r \leq f_{r,i}$ and $F_e\ (f_r) = 1$; if $f_r \geq f_{r,n}$. Fig. 21 shows the empirical cumulative curves obtained for P83 and P701 samples.

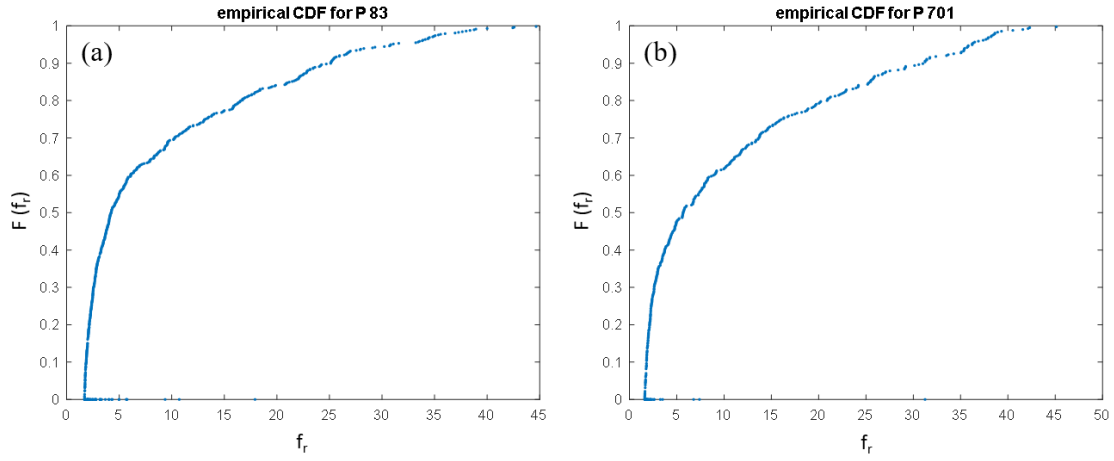

Figure 21: Empirical cumulative curves for P83 (a) and P701 (b) samples.

These figures show that their shapes are similar to an exponential distribution. The similarity itself is not enough to determine the exact type of distribution. Thus, many different types of distributions were examined, such as uniform, normal, exponential, Poisson, and Weibull distributions, and the Weibull distribution gave the best match with the calculated empirical cumulative curves, shown in Fig. 21. Moreover, the Weibull distribution is used to show the characteristics of many different types of distributions, therefore the data were analyzed based on Weibull statistics.

In material science the Weibull distribution [113] has been widely used in order to find which distribution function can fit the best the experimental data. The Weibull CDF and PDF are defined as:

$$F\ (\varepsilon) = 1 - \exp[-(\varepsilon/\lambda)^k] \tag{7}$$

$$f\ (\varepsilon) = \frac{\mathrm{d}F\ (\varepsilon)}{\mathrm{d}\varepsilon} = \frac{k}{\lambda}\left(\frac{\varepsilon}{\lambda}\right)^{k-1} \exp[-(\varepsilon/\lambda)^k] \tag{8}$$

where k is the shape parameter and λ stands for the scale parameter of the distribution. The shape parameter determines the shape of the Weibull curve. By varying k and consequently the shape of the function, one can model the characteristics of many different distributions. For example, if $k = 1$, the Weibull distribution yields the exponential distribution. With the aid of mechanical experiments performed on several electrospun PSI fiber texture, our main purpose is to determine the $F\ (\varepsilon)$ CDF. According to the best of our knowledge, no experimental result providing the distribution function for any fiber bundle is available in the scientific literature.

A Weibull plot was created for the sample, which is a special graphical technique to visualize whether the data actually follow the Weibull distribution. The plot was prepared based on the Eq. 7, which can be rearrange into the following equations:

$$-\ln\big(1 - F(\varepsilon)\big) = (\varepsilon/\lambda)^k \tag{9}$$

$$\ln[-\ln\big(1 - F(\varepsilon)\big)] = k\ln\varepsilon - k\ln\lambda \tag{10}$$

where $\ln[-\ln\big(1 - F(\varepsilon)\big)]$ gives the probability of the Weibull CDF on the y-axis and $\ln\varepsilon$ is the independent variable on the x-axis. If the data points in this ln-ln plot follow a linear or nearly linear curve, it yields estimate for the shape and the scale parameters of the Weibull distribution. According to the Eq. 10, the shape parameter (k) is the slope of the fitted line and the scale parameter (λ) is the exponent of the intercept. Fig. 22 shows the Weibull probability plot for P83 and P701 samples.

DOI:10.14753/SE.2022.2605

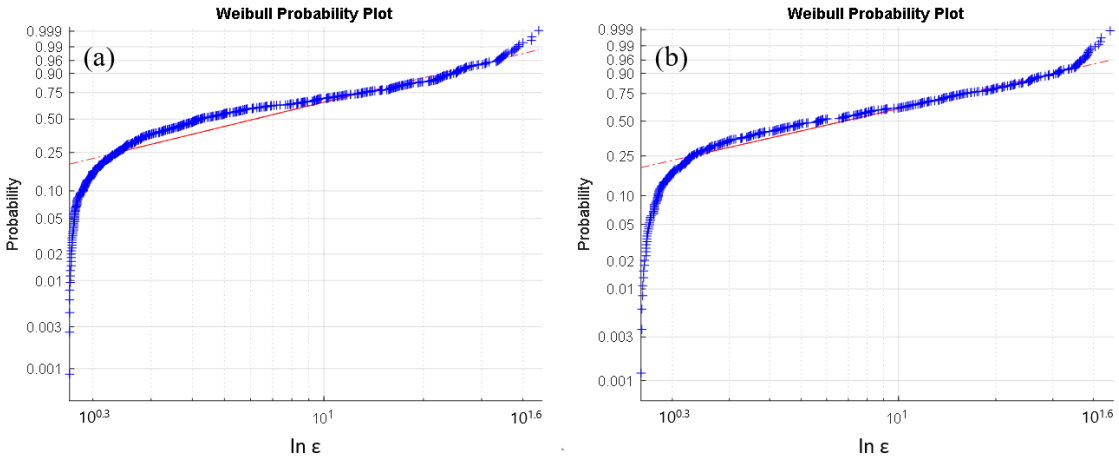

Figure 22: Weibull probability plot for P83 (a) and P701 (b) samples. The red solid line is the least square fitted line.

It can be seen that except some first and last data, the rest of the measured point fits fairly well on the straight line. At the beginning of the mechanical measurement, the possibility of error is still high, the sample is not yet properly stretched, and the machine sets the initial pulling distance with a pre-measurement, which can cause a significant deviation at the beginning of the curve. At the end of the mechanical measurement, the weak fibrous structure breaks, leaving only a few fibers, as a result of which the fluctuation of the measuring head increases and outstanding data can appear. For the P83 sample, the shape parameter was found to be: 0.97, for the P701 sample, shape parameter was found to be: 1.14. I have performed these calculations for the 20 different PSI fiber networks (see Table II). The data shows that the shape parameter, k scatter around unity. On the basis of statistical analyses, I have found for $k = 1.0 \pm 0.2$ (standard deviation). This means that the rupture force statistics for PSI electrospun polymer fibers, within the experimental accuracy, follow exponential probability distribution except some first and last data.

DOI:10.14753/SE.2022.2605

Table II: Initial stiffness (K_o) and shape parameter (*k*) obtained for PSI fiber textures

Sample code	Force at maximum	Extension at maximum	K_o	Δf_{error}	*k*
	N	mm	N/mm	mN/mm	-
P11	1.047	6.185	0.459	0.5	0.98
P12	0.672	6.003	0.303	1.5	1.1
P22	3.828	7.387	1.404	1.3	0.93
P41	2.163	10.812	0.542	2.0	0.95
P42	1.161	4.297	0.732	1.3	1.12
P43	3.866	9.218	1.137	1.5	0.89
P45	2.796	6.452	1.174	1.5	0.92
P46	1.992	4.897	1.102	2.0	0.91
P63	0.138	2.207	0.169	2.0	1.68
P71	0.288	12.795	0.061	2.0	1.15
P72	1.178	7.670	0.416	2.0	0.97
P81	0.911	7.855	0.314	1.8	0.96
P82	2.6	9.65	0.73	3.5	1.12
P83	0.645	5.685	0.307	1.5	0.97
P84	0.621	6.183	0.272	2.0	1.32
P85	0.220	8.475	0.070	1.4	1.39
P86	3.982	10.422	1.035	2.5	0.87
P87	4.268	3.355	3.447	3.5	0.93
P91	1.435	7.670	0.507	2	1.07
P701	0.748	5.97	0.341	2	1.14

This information provides a solid basis to get a deeper insight into the mechanism of elastic-plastic deformation of weak planar networks made of fibers. It also makes possible to develop a statistical model, based on the direct comparison of experimental results with such model simulation, which considers different breaking thresholds statistics, picked randomly from exponential probability distribution function.

4.4. Estimation of loading curve from exponential probability distribution function

According to the FBM, Eq. 2 tells us that the loading curve is related to the CDF. If we adopt the Weibull CDF, then we can write for the loading force, *f*:

$$f = K_0\,[1 - F\,(\varepsilon)]\,\varepsilon \;\text{ where }\; F\,(\varepsilon) = 1 - \mathrm{e}^{-(\varepsilon/\lambda)^k} \tag{11}$$

Thus, the loading curve can be expressed as follows:

$$f = K_0\,\varepsilon\,\mathrm{e}^{-(\varepsilon/\lambda)^k} \tag{12}$$

From this expression, we can arrive at the maximum loading capacity (the maximum of the loading curve), by solving the following equation:

$$\frac{\mathrm{d}f}{\mathrm{d}\varepsilon} = 0, \frac{\mathrm{d}^2 f}{\mathrm{d}\varepsilon^2} < 0 \tag{13}$$

We obtain for the maximum point:

$$f_{\max} = K_0\,\varepsilon_{\max}\,\mathrm{e}^{-1/k} \;\text{ and }\; \varepsilon_{\max} = \lambda\,k^{-1/k} \tag{14}$$

Combining these equations, the initial stiffness can be written as:

$$K_0 = \frac{f_{\max}}{\varepsilon_{\max}}\;\mathrm{e}^{1/k} \tag{15}$$

This is an important result, since the initial stiffness characterizes the quality and texture of a material. If there were no failure at all, the loading force would vary linearly with the extension according to the prediction of Hooke's law: $f = K_0\,\varepsilon$ as it is shown by dashed line in Fig. 23. Table II. shows that the initial stiffness varies in a wide range.

If we adopt the exponential statistics for the failure formation (k = 1), then the loading curve can be expressed as:

$$f = K_0\,\mathrm{e}^{-(\varepsilon/\varepsilon_{\max})}\,\varepsilon \tag{16}$$

From this equation we expect that it describes a continuous loading curve which does not show any abrupt drop in the force.

It is a challenging task to compare the prediction of Eq. 16 with real experiments. This comparison is shown in Fig. 23, where the dashed lines show the Hookean behavior if no failure occurred.

DOI:10.14753/SE.2022.2605

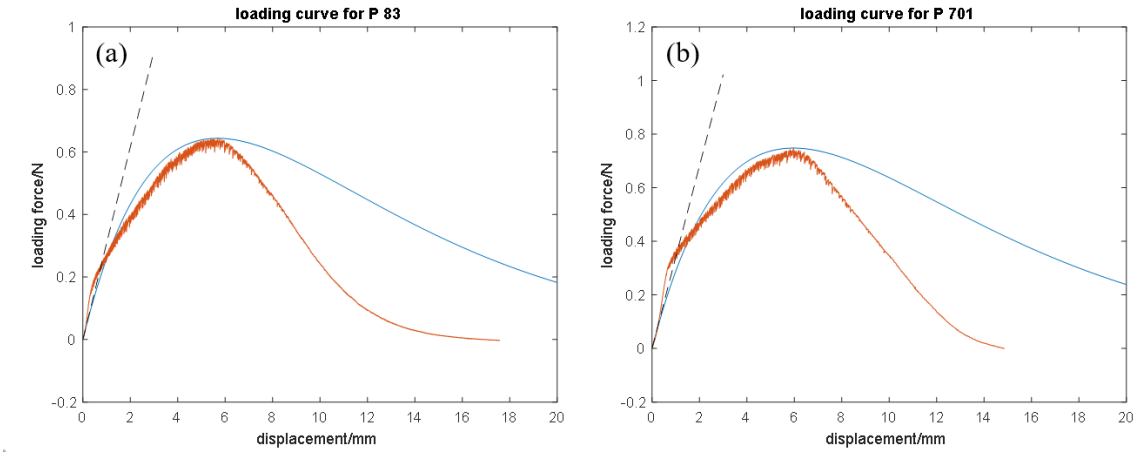

Figure 23: Comparison of calculated (blue) and measured (red) loading curve for P83 (a) and P701 (b) samples. The dashed line represents the mechanical behavior without failures.

It can be concluded that the theoretical loading curve fits satisfactorily to the experimental one until the maximum loading capacity is achieved, so at the increasing part of the curve the damage occurs mainly according to the FBM. Beyond the maximum point the two curves run separately, which is a typical finding for all the studied textures. This discrepancy suggests different failure mechanism when the maximum loading capacity is exceeded. In this part, the decreasing trend caused by ruptures does not follow the FBM, here the SBHL mechanism may come to the fore, the incorporation of which into the model requires further studies.

4.5. Typical loading curve of a biomaterial

Beside PSI samples, human biological material was also measured to investigate the relationship in the mechanical properties between the real human tissue and the PSI electrospun fiber networks. 5 mm wide rings were measured from a long piece of human arteria femoralis under physiological saline to provide similar circumstances as in the body. The loading curves of two randomly selected specimens can be seen in Fig. 24.

DOI:10.14753/SE.2022.2605

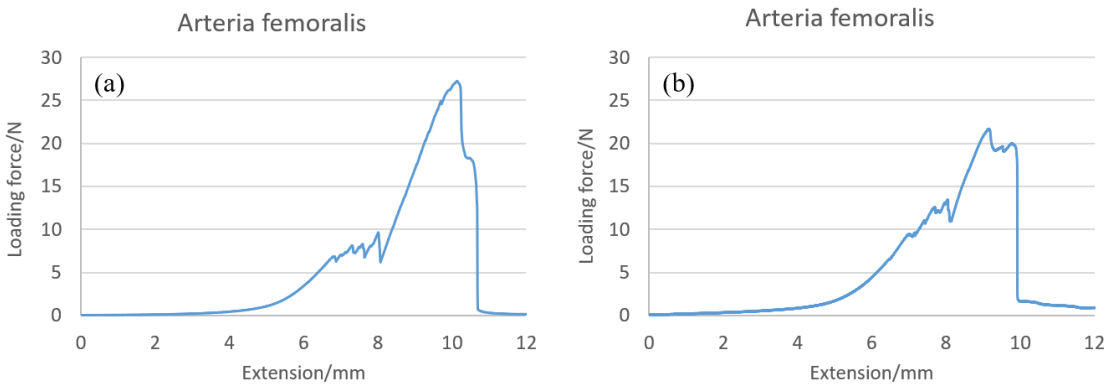

Figure 24: Load-extension curves of two arteria femoralis rings. These samples were cut from the same piece of human arteria femoralis.

In the load-extension curve of the arteria femoralis a saw-tooth like behavior can be seen, but, instead of a maximum type dependence, the loading curve shows a sudden breakage of the material around 10 mm extension. This shape is similar to the expected one according to the SBHL system mechanism. At the beginning the sample withstands tensile force due to its flexibility, and then as the extension increases the SB-s in the tissue break and the hidden lengths can be released, which cause the saw-tooth like behavior in the curve until the whole material damages and the force returns to zero.

Comparing the mechanical properties of PSI and human tissues, I found that the shape of the loading curve in macroscale is quite different, but many similarities can be discovered in microscale. According to these results, the PSI fibrous networks can be a good alternative in biomedical application as artificial tissue, and if we are able to understand the mechanical behavior of a polymer electrospun fiber mat, it can be modified according to our requirements to achieve the best resistance.

DOI:10.14753/SE.2022.2605

5. CONCLUSIONS

The motivation of this work was to understand the mechanical properties of planar, randomly oriented fiber mats.

With electrospinning technique, I successfully prepared fiber mats from PSI. The morphology investigation certified that the electrospun fibers have smooth surface and no fusion can be found between fibers. The average fiber size was found to be: 720±210 nm (standard deviation), and according to the analysis of SEM images, no definite orientation can be detected in the mats.

Based on several mechanical experiments, it was found that tensile property of the textures shows nonlinear stress-strain behavior; saw tooth-like force–extension behavior at short scale and parabolic type loading curve with a maximum at large scale. A general mechanical feature has been found: at the beginning the force has an approximate linear relationship in the low strain regime, then at higher elongation, the slope of this dependence is continuously decreasing and the stress reaches a maximum point, which corresponds the maximum loading capacity of the sample. After that point, as the extension increases, the force declines.

This complex, nonlinear stress-strain behavior is likely due to a stiffness reduction caused by damage formation, due to ruptures of adhesive fiber-fiber bonds or fibers' degradation. According to this mechanism, whenever a contact point in the mat experiences a force equal to or greater than its strength threshold, it breaks and results in redistribution of the local stress among the surviving neighboring texture elements. As a consequence of stiffness reduction, the fiber mat cannot recover its original dimensions. I suppose that the dominating factor in the failure is the fracture of the joints and contact points between the fibers. The number of force drops following each fiber rupture as well as their magnitude were measured and analyzed.

The mechanical behavior of this random structure is discussed in the framework of the FBM; which helps in analyzing the damage and fracture of disordered materials subjected to an external force. Despite the simplicity of the model, I have found good agreement between theory and experiments in the deformation range up to the maximum loading capacity is achieved. After the maximum point, the decreasing trend caused by ruptures does not follow the linear stretch modulus of the FBM, the introduction of a

nonlinear stretch modulus becomes necessary based on the SBHL model. Nonlinear stretch modulus to study the nonlinear elastic response has been introduced recently [114]. This approach may be useful as a starting point for the development of more complex mechanical models. This model predicts that the nonlinear elastic modulus may decrease as the axial stretch increases, reflecting softening in a material under increasing axial load.

This experimental method has the potential for the development of a statistical model based on direct comparison of experimental results with model simulations and can contribute to the design of high-performance fiber mats. However, further experimental studies on systematic variations of fiber texture combined with numerical simulations and statistical physics models on damage evolution are required. This work is the beginning of a new direction and further studies are needed, such as anisotropy, structure change, poisson ratio, mixed fiber systems, mechanical behavior of dry/wet/swollen samples, effect of surface properties, and so on.

DOI:10.14753/SE.2022.2605

6. SUMMARY

The goal of this work was to create a planar, randomly oriented fibrous structure and to perform a sensitive mechanical testing, which provided monitoring the rupture formation, determining the number of ruptures as well as the magnitude of rupture force.

The mechanical property was measured with unidirectional strain-controlled loading where the deformation of the fiber mats during stretching can be detected. The experimental loading curve shows a symmetrical parabolic type dependence at large scale and a saw tooth-like force–extension behavior at small scale. This unusual behavior can be explained by stiffness reduction caused by damage formation, thus as the elongation increases, the weakest fiber begins to rupture, followed by other fibers in the order of increasing strength. The randomly appearing damage formation was analyzed by measuring subsequent force drops as a consequence of rupture of fibers, and the complex phenomenon was quantified by determining the number and the magnitude of the force drops.

The mechanical behavior of this random structure is discussed in the framework of the FBM; which helps in analyzing the damage and fracture of disordered materials subjected to an external force. Statistical analysis based on the CDF evidenced that the force drops due to ruptures follow an exponential distribution function. The data were analyzed based on Weibull statistics to verify that data follows an exponential distribution. According to the FBM, the loading curve can be directly related to the cumulative distribution function of rupture force. Adopting the exponential distribution function, the initial stiffness, one of the important mechanical characteristics of the texture, can be determined, and provide an equation to approximate the loading curve.

A satisfactory agreement has been found between the theory and experiments in the deformation range up to the maximum loading capacity is achieved. However, beyond this point the two curves separates. This indicates different failure mechanism, when the maximum loading capacity is exceeded.

These results obtained here have relevance to understand the load bearing capacity in electrospun fibers, and provides information for several fibrous systems including complex fibrillary biological structures.

7. REFERENCES

1. F.K. Ko, J. Jovicic (2004) Modeling of Mechanical Properties and Structural Design of Spider Web, Biomacromolecules, Vol 5 (3):780-785.
2. E. Wirth and F.G. Barth (1992) Forces in the spider orb web, Journal of Comparative Physiology A, Vol 171 (3):359-371.
3. M. Denny (1976) The physical properties of spider's silk and their role in the design of orb-webs, J. Exp. Biol., Vol 65 (2):483 – 506.
4. M. Benzarti, M.B. Tkaya, C.P. Mattei, H. Zahouani (2011) Hair Mechanical Properties Depending on Age and Origin, Int. J. of Biotech. and Bioeng., Vol 5 (2).
5. I.P. Seshadri, B. Bhushan (2008) In situ tensile deformation characterization of human hair with atomic force microscopy, Acta Materialia, Vol 56 (4):774-781.
6. Y. Yu, W. Yang, B. Wang, M.A. Meyers (2017) Structure and mechanical behavior of human hair, Materials Science and Engineering: C, Vol 73, 152-163.
7. B.L. Smith, T.E. Schäffer, M. Viani, J.B. Thompson, N.A. Frederick, J. Kindt, A. Belcher, G.D. Stucky, D.E. Morse, P.K. Hansma (1999) Molecular mechanistic origin of the toughness of natural adhesives, fibres and composites, Nature, Vol 399, 761-763.
8. H. Oxlund, T.T. Andreassen (1980) The roles of hyaluronic acid, collagen and elastin in the mechanical properties of connective tissues, J.Anat., Vol 131 (4):611-620.
9. C. Tao, Y. Zhang, B. Li, L. Chen (2017) Hierarchical micro/submicrometer-scale structured scaffolds prepared via coaxial electrospinning for bone regeneration, J. Mater. Chem. B, Vol 5 (46):9219-9228.
10. K. Molnar, D. Juriga, P.M. Nagy, K. Sinko, A. Jedlovszky-Hajdu, M. Zrinyi (2014) Electrospun poly(aspartic acid) gel scaffolds for artificial extracellular matrix, Polymer International, Vol 63 (9):1608-1615.
11. V. Melissinaki, A.A. Gill, I. Ortega, M. Vamvakaki, A. Ranella, J.W. Haycock, C. Fotakis, M. Farsari, F. Claeyssens (2011) Direct laser writing of 3D scaffolds for neural tissue engineering applications, Biofabrication, Vol 3, 045005.

12. D. Juriga, K. Nagy, A. J.-Hajdu, K. P.-Kovach, Y.M. Chen, G. Varga, M. Zrinyi (2016) Biodegradation and Osteosarcoma Cell Cultivation on Poly(aspartic acid) Based Hydrogels, ACS Applied Materials & Interfaces, Vol 8 (36):23463-23476.
13. J. Svobodová, V. Proks, Ö. Karabiyik, A.C.Ç. Koyuncu, G.T. Köse, F. Rypáček, H. Studenovská (2017) Poly(amino acid)-based fibrous scaffolds modified with surface-pendant peptides for cartilage tissue engineering, J. Tissue Eng. Regen. Med., Vol 11 (3):831–842.
14. D. Juriga, E. Sipos, O. Hegedűs, G. Varga, M. Zrínyi, K.S. Nagy, A. Jedlovszky-Hajdú (2019) Fully amino acid-based hydrogel as potential scaffold for cell culturing and drug delivery, Beilstein Journal of Nanotechnology, Vol 10, 2579-2593.
15. A. Valizadeh, S.M. Farkhani (2014) Electrospinning and electrospun nanofibers, IET Nanobiotechnol., Vol 8 (2):83–92.
16. D. Kai, S.S. Liow, X.J. Loh (2014) Biodegradable polymers for electrospinning: Towards biomedical applications, Materials Science and Engineering C, Vol 45, 659–670.
17. A. Moheman, M.S. Alam, A. Mohammad (2016) Recent trends in electrospinning of polymer nanofibers and their applications in ultra thin layer chromatography, Advances in Colloid and Interface Science, Vol 229, 1-24.
18. Y. Mu, F. Wu, Y. Lu, L. Wei, W. Yuan (2014) Progress of electrospun fibers as nerve conduits for neural tissue repair, Vol 9 (12):1869-1883.
19. G. Jin, R. He, B. Sha, W. Li, H. Qing, R. Teng, F. Xu (2018) Electrospun three-dimensional aligned nanofibrous scaffolds for tissue engineering, Materials Science and Engineering C, Vol 92, 995-1005.
20. C. Picu, J.F. Ganghoffer (2020) Mechanics of Fibrous Materials and Applications, Physical and Modeling Aspects, CISM International Centre for Mechanical Sciences, Courses and Lectures, Vol 596.
21. M.M. Maciel, S. Ribeiro, C. Ribeiro, A. Francesko, A. Maceiras, J.L. Vilas, S. Lanceros-Méndez (2018) Relation between fiber orientation and mechanical properties of nano- engineered poly(vinylidene fluoride) electrospun composite fiber mats, Composites Part B: Engineering, Vol 139, 146-154.

22. S.F. Chou, K.A. Woodrow (2017) Relationships between mechanical properties and drug release from electrospun fibers of PCL and PLGA blends, Journal of the Mechanical Behavior of Biomedical Materials, Vol 65, 724-733.
23. S.R. Baker, S. Banerjee, K. Bonin, M. Guthold (2016) Determining the mechanical properties of electrospun poly-ε-caprolactone (PCL) nanofibers using AFM and a novel fiber anchoring technique, Materials Science and Engineering C, Vol 59, 203-212.
24. L.M. Vas (2006) Strength of Unidirectional Short Fiber Structures as a Function of Fiber Length, Journal of Comp. Mat., Vol 40 (19).
25. L.M. Vas, T. Czigany (2006) Strength Modeling of Two-component Hybrid Fiber Composites in case of Simultaneous Fiber Failures, Journal of Comp. Mat., Vol 40 (19).
26. R. Ghobeira, M. Asadian, C. Vercruysse, H. Declercq, N. De Geyter, R. Morent (2018) Wide-ranging diameter scale of random and highly aligned PCL fibers electrospun using controlled working parameters, Polymer, Vol 157, 19-31.
27. W.E. Teo, R. Gopal, R. Ramaseshan, K. Fujihara, S. Ramakrishna (2007) A dynamic liquid support system for continuous electrospun yarn fabrication, Polymer, Vol 48 (12):3400–3405.
28. J.W.S. Hearle, P. Grosberg, S. Backer (1969) Structural mechanics of fibers, yarns, and fabrics, Wiley-Interscience, Vol 1.
29. E. Smit, U. Bűttner, R.D. Sanderson (2005) Continuous yarns from electrospun fibers, Polymer, Vol 46 (8):2419–2423.
30. M.B. Bazbouz, G. K. Stylios (2008) Novel mechanism for spinning continuous twisted composite nanofiber yarns, Eur Polymer J, Vol 44 (1):1–12.
31. M. Alava, K. Niskanen (2006) The physics of paper, Rep. Prog. Phys., Vol 69, 669–723.
32. K.K. Chawla (1998) Fibrous Materials, Cambridge University Press.
33. H.L. Cox (1952) The elasticity and strength of papers and other fibrous materials, British Journal of Applied Physics, Vol 3, 72-79.
34. A. Atala (2012) Tissue engineering of reproductive tissues and organs, Fertility and sterility, Vol 98 (1):21-29.

35. A.D. Theocharisa, S.S. Skandalis, C. Gialeli, N.K. Karamanos (2016) Extracellular Matrix Structure, Advanced Drug Delivery Reviews, Vol 97, 4-27.
36. B.S. Kim, D.J. Mooney (1998) Development of biocompatible synthetic extracellular matrices for tissue engineering, Trends Biotechnol, Vol 16 (5):224–230.
37. C. Frantz, K.M. Stewart, V.M. Weaver (2010) The extracellular matrix at a glance, Journal of cell science, Vol 123 (24):4195-4200.
38. K.C. Clause, T.H. Barker (2013) Extracellular matrix signaling in morphogenesis and repair, Current opinion in biotechnology, Vol 24 (5):830-833.
39. J.M. Muncie, V.M. Weaver (2018) The Physical and Biochemical Properties of the Extracellular Matrix Regulate Cell Fate, Current Topics in Developmental Biology, Vol 130, 1-37.
40. T. Rozario, D.W. DeSimone (2010) The extracellular matrix in development and morphogenesis: a dynamic view, Dev. Biol., Vol 341 (1):126–140.
41. S.F. Badylak, D.O. Freytes, T.W. Gilbert (2009) Extracellular matrix as a biological scaffold material: Structure and function, Acta Biomaterialia, Vol 5 (1):1-13.
42. T. Woods, P.F. Gratzer (2005) Effectiveness of three extraction techniques in the development of a decellularized bone–anterior cruciate ligament–bone graft, Biomaterials, Vol 26 (35):7339–7349.
43. J.S. Cartmell, M.G. Dunn (2004) Development of cell-seeded patellar tendon allografts for anterior cruciate ligament reconstruction, Tissue Eng., Vol 10 (7–8):1065–1075.
44. T.W. Gilbert, M.S. Sacks, J.S. Grashow, S.L-Y. Woo, S.F. Badylak, M.B. Chancellor (2006) Fiber kinematics of small intestinal submucosa under biaxial and uniaxial stretch, J Biomech. Eng., Vol 128 (6):890–898.
45. Z. Wang, C. Wang, C. Li, Y. Qin, L. Zhong, B. Chen, Z. Li, H. Liu, F. Chang, J. Wang (2017) Analysis of factors influencing bone ingrowth into three-dimensional printed porous metal scaffolds: A review, Journal of Alloys and Compounds, Vol 717, 271-285.

46. X. Shen, G. Zhao, L. Fan, Z. Guo, C. Zhao, A. Chen, G. Yang, Z. Cheng, N. Zhang (2020) CuO-C modified glass fiber films with a mixed ion and electron-conducting scaffold for highly stable lithium metal anodes, Journal of Materials Chemistry A, Vol 8, 21961-21967.
47. E. Aerts, J. Li, M.J. Van Steenbergen, T. Degrande, J.A. Jansen, X.F. Walboomers (2020) Porous titanium fiber mesh with tailored elasticity and its effect on stromal cells, J. of Biomed. Mater. Research Part B, Vol 108 (5):2180-2191.
48. D.M. Wilson, L.R. Visser (2001) High performance oxide fibers for metal and ceramic composites, Composites Part A, Vol 32 (8):1143-1153.
49. R. Yuan, X. Fu, X. Wang, P. Liu, L. Wu, Y. Xu, X. Wang, Z. Wang (2006) Template Synthesis of Hollow Metal Oxide Fibers with Hierarchical Architecture, Chem. Mater., Vol 18 (19):4700-4705.
50. M. Macías, A. Chacko, J.P. Ferraris, K.J. Balkus Jr. (2005) Electrospun mesoporous metal oxide fibers, Microporous and Mesoporous Materials, Vol 86 (1–3):1-13.
51. F.T. Wallenberger (2009) Commercial and Experimental Glass Fibers, Fiberglass and Glass Technology, 3-90.
52. T. Deák, T Czigány (2009) Chemical Composition and Mechanical Properties of Basalt and Glass Fibers: A Comparison, Textile Research Journal, Vol 79 (7):645-651.
53. S. Jiang, D. Han, C. Huang, G. Duan, H. Hou (2018) Temperature-induced molecular orientation and mechanical properties of single electrospun polyimide nanofiber, Materials Letters, Vol 216, 81-83.
54. T. An, B. Pant, S.Y. Kim, M. Park, S.J. Park, H.Y. Kim (2017) Mechanical and optical properties of electrospun nylon-6,6 nanofiber reinforced cyclic butylene terephthalate composites, J. of Ind. and Eng. Chem., Vol 55, 35-39.
55. Y. Li, C.T. Lim, M. Kotaki (2015) Study on structural and mechanical properties of porous PLA nanofibers electrospun by channel-based electrospinning system, Polymer, Vol 56, 572-580.

56. F. Aslani, F. Hamidi, A. Valizadeh, A. Thanh-Nhan Dang (2020) High-performance fibre-reinforced heavyweight self-compacting concrete: Analysis of fresh and mechanical properties, Const. and Build. Mat., Vol 232, 117230.
57. E. Schaal (1871) Über einige aus Asaparaginsäure entstehende Producte, Ann. Chem., Vol 157, 24-34.
58. H. Schiff (1897) Über Polyaspartsauren, Ber. dtsch. Chem., Vol 30, 2449.
59. M. Frankel, A. Berger (1951) Synthesis of Polyaspartic Acid, J. Org. Chem., Vol 16, 1513.
60. K. Harada (1959) Polycondensation of Thermal Precursors of Aspartic Acid, J. Org. Chem., Vol 24, 1662.
61. J. Kovács, I. Könyves, A. Pusztai (1953) Darstellung von Polyasparaginsäuren (Polyaspartsäuren) aus dem thermischen Autokondensations produkt der Asparaginsäure, Experientia, Vol 12, 459.
62. E. Jalalvandi, A. Shavandi (2018) Polysuccinimide and its derivatives: Degradable and water soluble polymers (review), European Polymer Journal, Vol 109, 43-54.
63. C.J. Thompson, G.G. Chase, A.L. Yarin, D.H. Reneker (2007) Effects of parameters on nanofiber diameter determined from electrospinning model, Polymer, Vol 48 (23):6913–6922.
64. T. Subbiah, G.S. Bhat, R.W. Tock, S. Parameswaran, S.S. Ramkumar (2005) Electrospinning of nanofibers, J. Appl. Polym. Sci., Vol 96 (2):557–569.
65. Q.P. Pham, U. Sharma, A.G. Mikos (2006) Electrospinning of polymeric nanofibers for tissue engineering applications: a review, Tissue Eng., Vol 12 (5):1197–1211.
66. A. Arinstein, E. Zussman (2011) Electrospun polymer nanofibers: Mechanical and thermodynamic perspectives, Journal of Polymer Science Part B. Polymer Physics, Vol 49 (10):691-707.
67. U. Stachewicz, F. Hang, A.H. Barber (2014) Adhesion Anisotropy between Contacting Electrospun Fibers, Langmuir, Vol 30 (23):6819−6825.
68. K. Molnar, L.M. Vas, T. Czigany (2012) Determination of tensile strength of electrospun single nanofibers through modeling tensile behavior of the nanofibrous mat, Composites Part B: Engineering, Vol 43 (1):15-21.

69. M.S. Fernandez, K. Passalacqua, J.I. Arias, J.L. Arias (2004) Partial biomimetic reconstitution of avian eggshell formation, J. Struct. Biol., Vol 148 (1):1–10.
70. D.R. Katti, K.S. Katti, J.M. Sopp, M. Sarikaya (2001) 3D finite element modeling of mechanical response in nacre-based hybrid nanocomposites, Comput. Theor. Polym. Sci., Vol 11 (5):397–404.
71. K. Okumura, P.G. de Gennes (2001) Why is nacre strong? Elastic theory and fracture mechanics for biocomposites with stratified structures, Eur. Phys. J. E., Vol 4, 121–127.
72. P. Fratzl, I. Burgert, H.S. Gupta (2004) On the role of interface polymers for the mechanics of natural polymeric composites, Phys. Chem. Chem. Phys., Vol 6 (24):5575–5579.
73. G.E. Fantner, E. Oroudjev, G. Schitter, L.S. Golde, P. Thurner, M.M. Finch, P. Turner, T. Gutsmann, D.E. Morse, H. Hansma, P.K. Hansma (2006) Sacrificial Bonds and Hidden Length: Unraveling Molecular Mesostructures in Tough Materials, Biophysical Journal, Vol 90 (4):1411-1418.
74. B.L. Smith, T.E. Schäffer, M. Viani, J.B. Thompson, N.A. Frederick, J. Kindt, A. Belcher, G.D. Stucky, D.E. Morse, P.K. Hansma (1999) Molecular mechanistic origin of the toughness of natural adhesives, fibres and composites, Nature, Vol 399, 761-763.
75. P.K. Hansma, G.E. Fantner, J.H. Kindt, P.J. Thurner, G. Schitter, P.J. Turner, S.F. Udwin, M.M. Finch (2005) Sacrificial bonds in the interfibrillar matrix of bone, J. Musculoskelet Neuronal Interact, Vol 5 (4):313-315.
76. G.E. Fantner, T. Hassenkam, J.H. Kindt, J.C. Weaver, H. Birkedal, L. Pechenik, J.A. Cutroni, G.A.G. Cidade, G.D. Stucky, D.E. Morse, P.K. Hansma (2005) Sacrificial bonds and hidden length dissipate energy as mineralized fibrils separate during bone fracture, Nature Materials, Vol 4 (8):612-616.
77. J.B. Thompson J.H. Kindt, B. Drake, H.G. Hansma, D.E. Morse, P.K. Hansma (2001) Bone indentation recovery time correlates with bond reforming time, Nature, Vol 414, 773-776.
78. M.E. Launey, M.J. Buehler, R.O. Ritchie (2010) On the Mechanistic Origins of Toughness in Bone, Annu. Rev. Mater. Res., Vol 40, 25-53.

79. M.J. Buehler, S. Keten (2010) Failure of molecules, bones, and the Earth itself, Rev. Mod. Phys., Vol 82, 1459.
80. J.D. Currey (1977) Mechanical properties of mother of pearl in tension, Proc. R. Soc. Lond. B, Vol 196, 443.
81. A.P. Jackson, J.F.V. Vincent, R.M. Turner (1988) The mechanical design of nacre, Proc. R. Soc. Lond. B, Vol 234, 415.
82. I.C. Gebeshuber, J.H. Kindt, J.B. Thompson, Y. Del Amo, H. Stachelberger, M.A. Brzezinski, G.D. Stucky, D.E. Morse, P.K. Hansma (2003) Atomic force microscopy study of living diatoms in ambient conditions, J. Microsc., Vol 212 (3)292-299.
83. M.J. Higgins, S.A. Crawford, P. Mulvaney, R. Wetherbee (2002) Characterization of the adhesive mucilages secreted by live diatom cells using atomic force microscopy, Protist, Vol 153, 25-38.
84. A. Sarkar, S. Caamano, J.M. Fernandez (2007) The Mechanical Fingerprint of a Parallel Polyprotein Dimer, Biophys. J., Vol 92 (4):L36-L38.
85. E. Oroudjev, J. Soares, S. Arcdiacono, J.B. Thompson, S.A. Fossey, H.G. Hansma (2002) Segmented nanofibers of spider dragline silk: atomic force microscopy and single-molecule force spectroscopy, Proc. Natl. Acad. Sci. USA, Vol 99 (2):6460–6465.
86. P. Bianco, A. Nagy, A. Kengyel, D. Szatmári, Zs. Mártonfalvi, T. Huber, M.S.Z. Kellermayer (2007) Interaction forces between F-actin and titin PEVK domain measured with optical tweezers, Biophysical Journal, Vol 93 (6):2102-2109.
87. G. Xu, L. Gong, Z. Yang, X.Y. Liu (2014) What makes spider silk fibers so strong? From molecular-crystallite network to hierarchical network structures, Soft Matter, Vol 10 (13):2116-2123.
88. A.E. Elbanna, J.M. Carlson (2013) Dynamics of Polymer Molecules with Sacrificial Bond and Hidden Length Systems: Towards a Physically-Based Mesoscopic Constitutive Law, PLoS ONE, Vol 8 (4):e56118.
89. N. Holten-Andersen, G.E. Fantner, S. Hohlbauch, J.H. Waite, F.W. Zok (2007) Protective coatings on extensible biofibres, Nat. Mater., Vol 6, 669-672.

90. N. Holten-Andersen, T.E. Mates, M.S. Toprak, G.D. Stucky, F.W. Zok, J.H. Waite (2009) Metals and the Integrity of a Biological Coating: The Cuticle of Mussel Byssus, Langmuir, Vol 25 (6):3323-3326.
91. G.E. Fantner, J. Adams, P. Turner, P.J. Thurner, L.W. Fisher, P.K. Hansma (2007) Nanoscale Ion Mediated Networks in Bone: Osteopontin Can Repeatedly Dissipate Large Amounts of Energy, Nano Lett., Vol 7 (8):2491-2498.
92. C.K.C. Lieou, A.E. Elbanna, J.M. Carlson (2013) Sacrificial bonds and hidden length in biomaterials – a kinetic, constitutive description of strength and toughness in bone, Physical Review E - Statistical, Nonlinear, and Soft Matter Physics, Vol 88 (1):012703.
93. G.I. Barenblatt (1962) Mathematical theory of equilibrium cracks in brittle fracture, Advances in Applied Mechanics, Vol 7, 55–129.
94. X.P. Xu, A. Needleman (1993) Void nucleation by inclusion debonding in a crystal matrix, Materials Science and Engineering, Vol 1 (2):111–132.
95. T.M. Dugdale, R. Degastine, A. Chiovitti, P. Mulvaney, R. Wetherbee (2005) Single adhesive nanofibers from a live diatom have the signature fingerprint of modular proteins, Biophysical Journal, Vol 89 (6):4252–4260.
96. N. Becker, E. Oroudjev, S. Mutz, J.P. Cleveland, P.K. Hansma, C.Y. Hayashi, D.E. Makarov, H.G. Hansma (2003) Molecular nanosprings in spider capture-silk threads, Nature Materials, Vol 2, 278–283.
97. M.A. Hartmann, P. Fratzl (2009) Sacrificial Ionic Bonds Need To Be Randomly Distributed To Provide Shear Deformability, Nano Lett., Vol 9 (10):3603-3607.
98. R.K. Nallaa, J.J. Kruzica, J.H. Kinney, R.O. Ritchie (2004) Effect of aging on the toughness of human cortical bone: evaluation by R-curves, Bone, Vol 35, 1240-1246.
99. M. Gass, B. Dawson-Hughes (2006) Preventing osteoporosis-related fractures: an overview, Am. J. Med., Vol 119 (4):S3–S11.
100. F.T. Peirce (1926) Tensile tests for cotton yarns. 'the weakest link' theorems on the strength of long composite specimens, J. Textile Inst., Vol 17, T355–368.
101. A.H. Hansen, P.C. Hemmer, S. Pradhan (2015) The Fiber Bundle Model: Modeling Failure in Materials, Wiley-VCH Verlag GmbH and Co., KGaA.

102. H.E. Daniels (1945) The statistical theory of the strengths of bundles of threads, Proc. R. Soc. London, Ser. A, Vol 183, 405-435.
103. B.D. Coleman (1956) Time dependence of mechanical breakdown phenomena, J. Appl. Phys., Vol 27, 862.
104. S. Zapperi, A. Vespignani, H.E. Stanley (1997) Plasticity and avalanche behavior in microfacturing phenomena, Letters to Nature, Vol 388.
105. W.L. Martinez, A.R. Martinez (2016) Computer Science and Data Analysis Series: Computational Statistics Handbook with MATLAB, 3rd Edition, CRC Press Taylor and Francis Group, Chapman and Hall Book.
106. What is FFT in ImageJ: https://imagejdocu.tudor.lu/gui/process/fft#fft1 (Letöltés: 2021.09.25)
107. Code of FFT in ImageJ, by Arlo Reeves: https://imagej.nih.gov/ij/plugins/download/FFT_.java (Letöltés: 2021.09.25)
108. A.N. Natali, P.G. Pavan, E.L. Carniel, M.E. Lucisano, G. Taglialavoro (2005) Anisotropic elasto-damage constitutive model for the biomechanical analysis of tendons, Medical Engineering and Physics, Vol 27, 209-214.
109. M.W. Lee, S. Sett, S.S. Yoon, A.L. Yarin (2016) Self-healing of nanofiber-based composites in the course of stretching, Polymer, Vol 103, 180-188.
110. P. Isakson, R. Hagglung (2007) Evolution of bond fractures in a randomly distributed fiber network, International Journal of Solids and Structures, Vol 44, 6135-6147.
111. E. Sipos, T. Kaneko, M. Zrinyi (2019) Experimental Investigation of Damage Formation in planar Fibrous Networks During stretching, Scientific Reports, 9:2816.
112. E. Sipos, A. Juhasz, M. Zrinyi (2021) Characteristic load-elongation behavior of weak electrospun fiber texture, Journal of Molecular Liquids, Vol 329, 115459.
113. W. Weibull (1951) A Statistical Distribution Function of Wide Applicability, Journal of Applied Mechanics, Vol 18, 293-297.
114. L.A. Mihai, A. Goriely (2017) How to characterize a nonlinear elastic material? A review on nonlinear constitutive parameters in isotropic finite elasticity, Proc.R.Soc. A, Vol 473, 2207.

DOI:10.14753/SE.2022.2605

8. LIST OF PUBLICATIONS

8.1. Publications relevant to the Ph.D. thesis

1. E. Sipos, T. Kaneko, M. Zrinyi (2019) Experimental Investigation of Damage Formation in planar Fibrous Networks During stretching, Scientific Reports, 9:2816.
2. E. Sipos, A. Juhasz, M. Zrinyi (2021) Characteristic load-elongation behavior of weak electrospun fiber texture, Journal of Molecular Liquids, Vol 329, 115459.

8.2. Other publications

1. D. Juriga, E. Sipos, O. Hegedűs, G. Varga, M. Zrínyi, K.S. Nagy, A. Jedlovszky-Hajdú (2019) Fully amino acid-based hydrogel as potential scaffold for cell culturing and drug delivery, Beilstein Journal of Nanotechnology, Vol 10, 2579-2593.
2. O. Hegedűs, D. Juriga, E. Sipos, C. Voniatis, A. Juhasz, A. Idrissi, M. Zrínyi, G. Varga, A. Jedlovszky-Hajdú, K.S. Nagy (2019) Free thiol groups on poly(aspartamide) based hydrogels facilitate tooth-derived progenitor cell proliferation and differentiation, PLoS ONE, Vol 14 (12): e0226363.

DOI:10.14753/SE.2022.2605

9. ACKNOWLEDGEMENTS

First of all, I would like to express my deepest gratitude to my supervisor, Prof. Miklós Zrínyi, for his support, guidance and encouragement during my Ph.D. work.

I would like to offer my gratitude to Prof. Miklós Kellermayer, director of Department of Biophysics and Radiation Biology, who supported my work by enabling the availability of the instruments located in the institute, and to all colleagues from Department of Biophysics and Radiation Biology for their useful suggestions.

I must also acknowledge the received spiritual support and a lot of practical help in the laboratory from my colleagues at the Laboratory of Nanochemistry, Angéla Jedlovszky-Hajdú, Dóra Barczikai, Constantinos Voniatis, Rita Varga, Krisztina Tóth, and Dávid Juriga.

Special thanks should be given to my great colleague Ákos Juhász for his constructive suggestions, and his help in the evaluation of the measurements.

I also acknowledge the financial support of the Károly Rácz Clinical Medicine Doctoral School of Semmelweis University thus enabling this work to take place.

Last but not least, my biggest thanks go to my husband, Péter Forró, who has always listened to my concerns, and given me all the support I need to overcome my fears and finish my Ph.D. work. For me, the spiritual strength he provided was the most I could get during these four years.